# Mysteries of Engineering Fluid Mechanics

Gordon D. Stubley
Mechanical Engineering Department
University of Waterloo
Waterloo ON N2L 3G1
CANADA
email: stubley@uwaterloo.ca

November 30, 2003

# Contents

# List of Figures

# Preface

One of the realities of the flow of fluids found in most industrial settings, is that the flow patterns and physics are much more complex than those of the model flows presented in undergraduate texts on engineering fluid mechanics. The chapters that follow give you an opportunity to increase your ability to understand and control these complex fluid flows.

Each chapter is presented as a mystery which is unraveled as the chapter progresses. The unraveling of the mystery will involve an exploration of actual flows that can be easily set up and virtual flow fields obtained by computer simulation using computational fluid dynamics (CFD) technology.

The presentation of each mystery has been designed to give ample opportunity for you to solve the mystery by exploring the flow fields. Take the time to see all of the features in each flow and to identify the relevant flow kinematics, forces, and dynamics.

Best wishes for an enjoyable learning experience.

# Chapter 1

# The Fate of Sinking Tea Leaves

## 1.1 The Mystery

Tea leaves are added to a beaker of still cold water. As the leaves get soggy, they begin to sink to the bottom of the beaker. This indicates that the tea leaves are heavier than water.

After most of the leaves have sunk to the bottom, the water in the beaker is stirred in either a clockwise or counter-clockwise direction. Where will the leaves on the bottom of the beaker collect - near the outer wall or near the middle?

Those of you that set up this simple flow will notice that the tea leaves tend to move towards the middle of the beaker. Why doesn't centrifugal action throw the leaves towards the outer wall?

## 1.2 Model Flow 1

### 1.2.1 Description of Flow Conditions

One of the simplest imaginable spinning flows is that of a large region of fluid spinning with a uniform angular velocity, $\omega$ about the $z$ axis. The fluid is above a large fixed plate that lies in the $x-y$ plane as shown in Figure 1.1.

It is natural to use a cylindrical $r-\theta-z$ coordinate system for spinning flows where the $z$ axis coincides with the axis of rotation. The three components of the velocity in this coordinate system are the radial, $V_r$, tangential, $V_t$, and the axial, $V_a$ velocities in the $r, \theta$ and $z$ directions, respectively. A
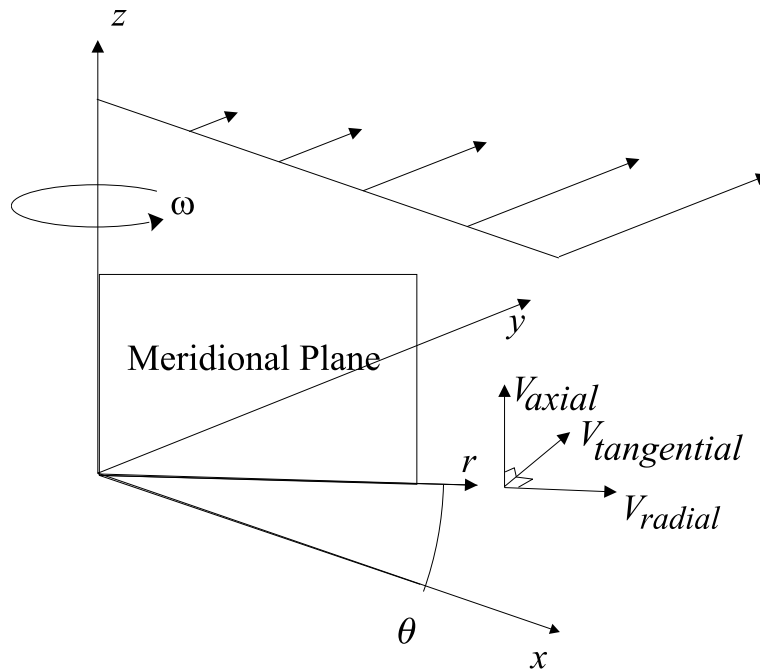
Figure 1.1: Geometry of infinite spinning fluid above fixed plate.

meridional plane is a plane which contains the axis of rotation and is swept around that axis.

The pictures which follow show the flow of water with nominal STP properties in a region which extends radially from the axis of rotation to a radius of $0.025[m]$ and vertically from the plate to a height of $0.01[m]$. The density and dynamic viscosity of the water are $1000[kg\ m^{-3}]$ and $1.0 \times 10^{-3}[kg\ m^{-1}s^{-1}]$, respectively. The rotation rate is $1[rad\ s^{-1}]$ or just under $10[rpm]$. The simulated velocity and pressure fields are presented on a uniform mesh with 11 nodes in the radial direction (node spacing of $\Delta r = 0.0025[m]$) and with 21 nodes in the axial direction (node spacing of $\Delta z = 0.0005[m]$).

### 1.2.2 Exploration

**Kinematic Features**

Figure 1.2 shows the three-dimensional velocity vectors plotted on the $x - z$ meridional plane. For this flow, it is sufficient to focus on a meridional plane because the flow field does not vary in the tangential direction. Can you see the rotational nature of the velocity field? What other characteristics of the velocity field can you discern from this figure?

Did you notice that:

- the velocity along the top is almost aligned with the tangential direction and varies linearly as expected for solid body rotation. Note that $v_t = \omega r$ so that at the outer edge the tangential velocity is $0.025[m\ s^{-1}]$ as indicated by the red colour of the velocity vectors near the outer top corner of the region;

- the velocity field becomes independent of distance in the axial direction (or in other words the axial gradient of the velocity approaches zero, $\frac{\partial \vec{V}}{\partial z} \approx 0$) far above the fixed plate,

- the tangential velocity goes to zero as the plate is approached indicating that the no-slip condition prevails on the plate,

- the layer of fluid immediately above the fixed plate is moving towards the axis of rotation. This negative radial velocity component is largest near the outer edge and decreases towards the axis of rotation;

- there is a layer of fluid in the middle which appears to be moving away from the axis of rotation, and

- the shape of each column of velocity vectors is similar?

Figure 1.3 shows a two-dimensional plot of the radial and axial velocity components on the $x - z$ meridional plane. Use this meridional plot to discover more detail about the radial flow observed above. How strong is the radial flow? Is the velocity far above the fixed plate strictly in the tangential direction?

With this level of detail, you should now notice that:

- the magnitude of the maximum flow in the meridional plane is just below $0.015[m\ s^{-1}]$ or just under half of the maximum tangential speed,
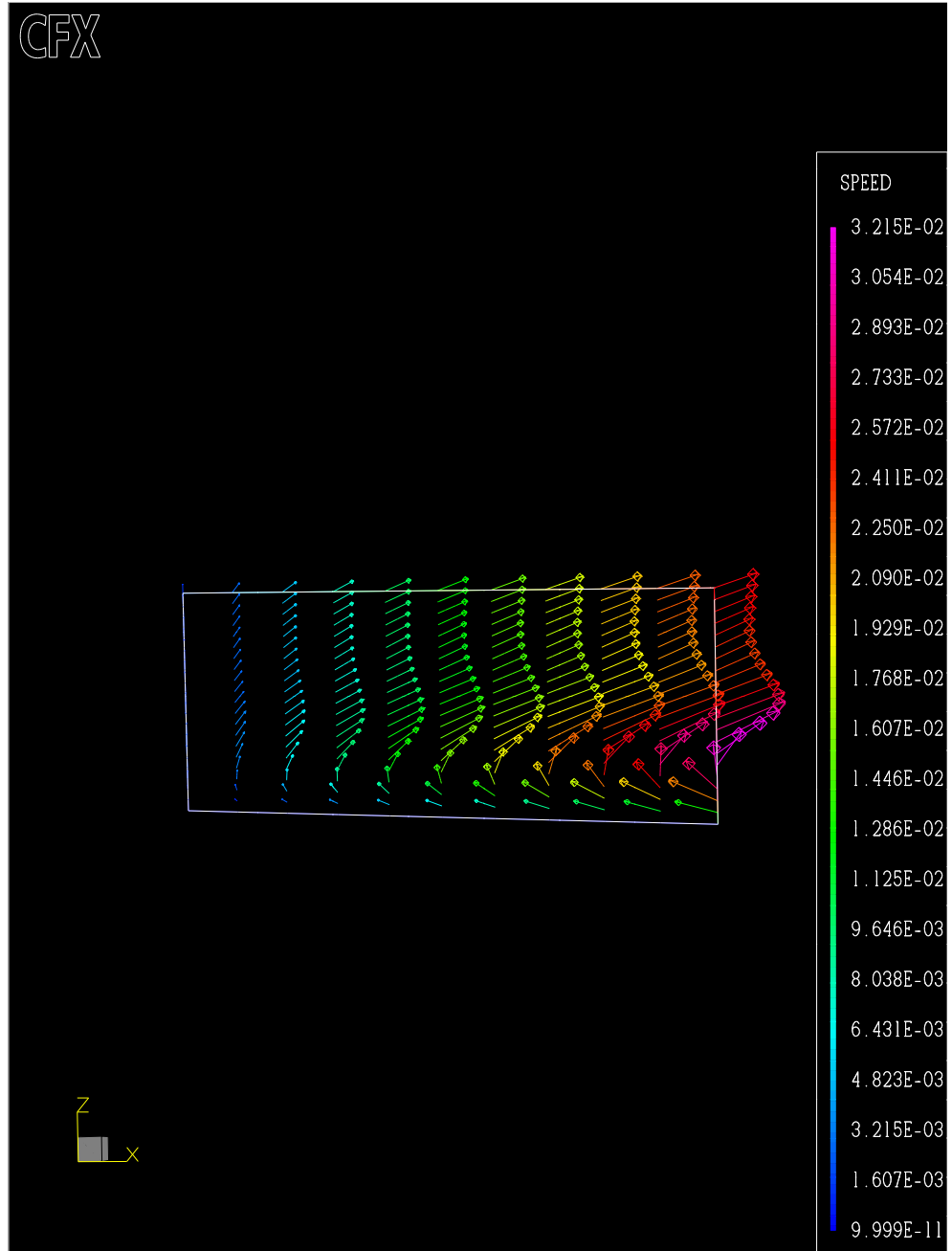
Figure 1.2: Velocity vectors at the nodes on the $x - z$ meridional plane
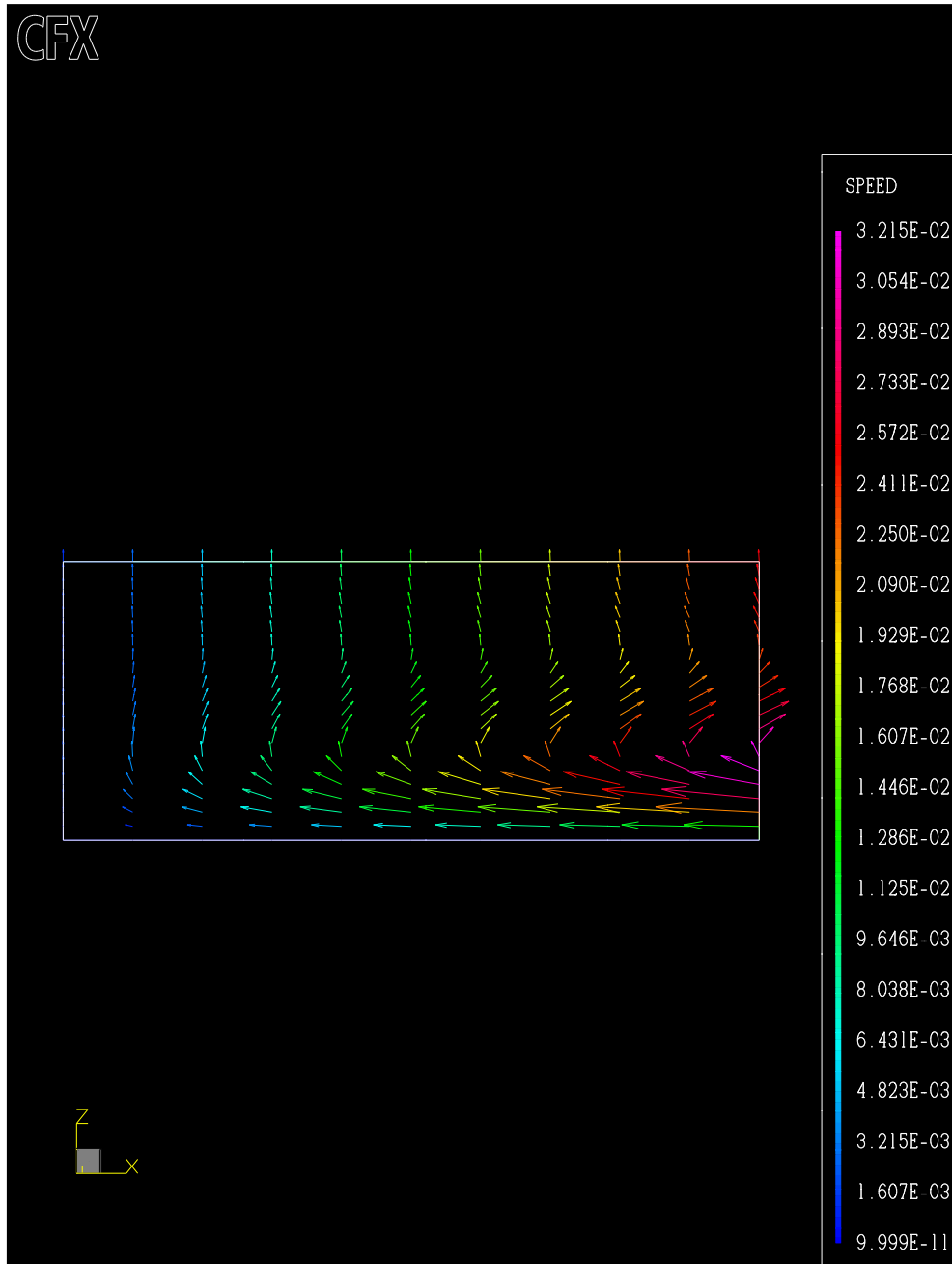
Figure 1.3: Meridional plane velocity vectors at the nodes on the $x - z$ meridional plane

- the radial flow, both towards and away from the axis of rotation, is clearly seen, and

- an axial velocity component develops with distance above the plate. Far from the plate, the axial velocity component becomes independent of both radial and axial positions.

These pictures show that there are two views of the velocity field: the top view of a horizontal rotating flow and the side view of flow moving radially and axially. This radial/axial flow is known as a *secondary flow*. The net velocity field is the superposition of these two views: a velocity field which has the dominant solid body rotation portion with a *secondary flow*.

Figure 1.4 shows the three-dimensional nature of the flow. Streamlines starting near the plate on the far left of the flow domain spiral towards the centreline and upwards as a result of the rotating and secondary flows. This flow pattern is consistent with the observation that the heavy tea leaves collected near the centreline at the bottom of the beaker.
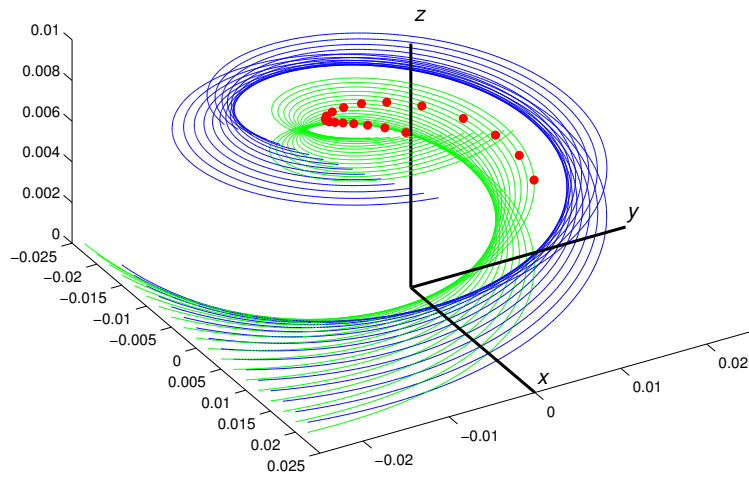


Figure 1.4: Streamlines of rotational flow over an infinite fixed plate.

### Dynamic Features

The kinematic views of the flow field show that even though the flow geometry and conditions are very simple, the flow pattern is surprisingly complex.

What causes this complexity?
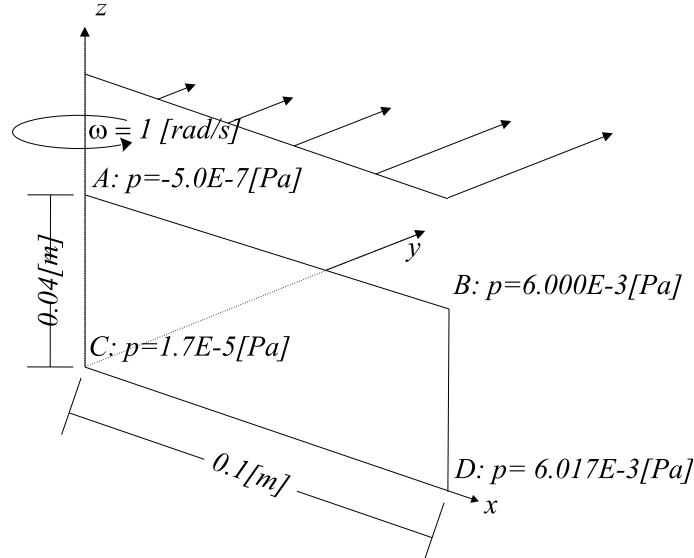


Figure 1.5: Layout of four points of pressure in the $x - z$ meridional plane.

Figure 1.5 shows the layout of the $x-z$ meridional plane with four points at the corners of the region of interest. Points A and B are in the far field region well above the fixed plate and points C and D are in the near plate region. The fringe plot in Figure 1.6 shows the pressure distribution in the $x - z$ plane. The values of the pressure in the four corner points are also included in Figure 1.5.

These two figures show the following features of the pressure field in this flow:

- The nearly rectangular pressure colour bars in Figure 1.6 indicate that the pressure gradient in the radial direction is significantly greater than the gradient in the axial direction;

- The decreasing widths of the pressure colour bars in Figure 1.6 indicate that the radial pressure gradient increases with radial distance from the axis of rotation;

- The global radial and axial pressure gradients are $\frac{\Delta p}{\Delta r} \approx 12.5 [Pa\ m^{-1}]$ and $\frac{\Delta p}{\Delta z} \approx -0.096 [Pa\ m^{-1}]$, respectively. This confirms that the radial pressure gradient dominates.
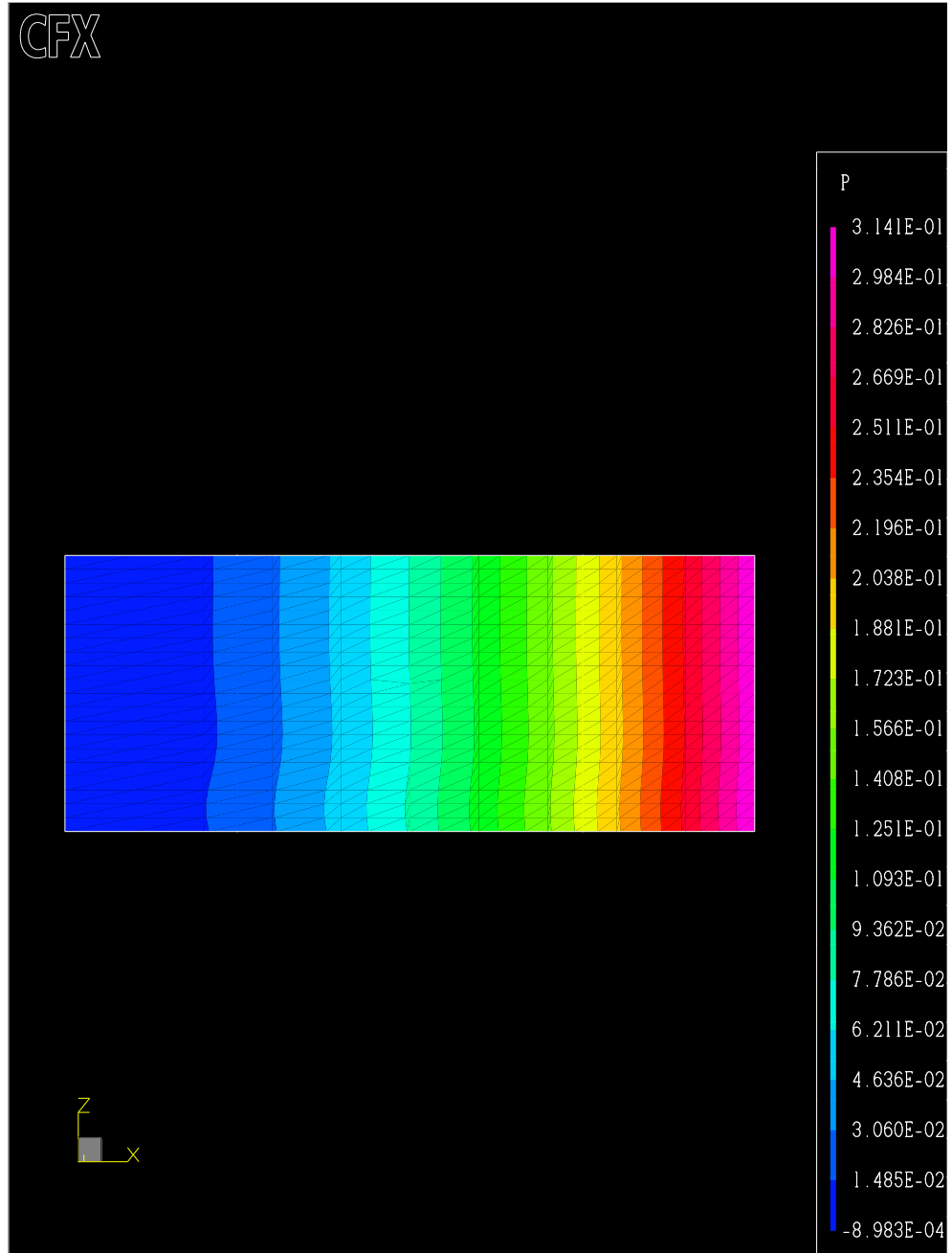
Figure 1.6: Fringe plot of pressure on the on the $x - z$ meridional plane.

The connection between the pressure gradient and the velocity field can be seen in the radial momentum equation written in cylindrical coordinates:

$$\rho\frac{\partial v_r}{\partial t} + \rho v_r\frac{\partial v_r}{\partial r} + \rho\frac{v_t}{r}\frac{\partial v_r}{\partial \theta} + \rho v_a\frac{\partial v_r}{\partial z} - \rho\frac{v_t^2}{r}$$
$$= -\frac{\partial p}{\partial r} +$$
$$\mu\left[\frac{1}{r}\frac{\partial}{\partial r}\left(r\frac{\partial v_r}{\partial r}\right) + \frac{1}{r^2}\frac{\partial}{\partial \theta}\left(\frac{\partial v_r}{\partial \theta}\right) + \frac{\partial}{\partial z}\left(\frac{\partial v_r}{\partial z}\right) - \frac{v_r}{r^2} - \frac{2}{r^2}\frac{\partial v_t}{\partial \theta}\right] \quad (1.1)$$

Throughout the flow domain, the flow field has the following properties:

- the flow is steady, $\frac{\partial}{\partial t} \approx 0$, and

- there is no variation of pressure or velocity in the tangential direction, $\frac{\partial}{\partial \theta} \approx 0$.

In the far field region(i.e. between Points A and B in Figure 1.5) the velocity gradients in the axial direction are negligible, $\frac{\partial \vec{V}}{\partial z} \approx 0$. Therefore, in the far field region the radial momentum balance reduces to:

$$-\rho\frac{v_t^2}{r} = -\frac{\partial p}{\partial r} \quad (1.2)$$

or in other words, the radial pressure gradient solely balances the centrifugal acceleration of the tangential velocity field.

Since the tangential velocity is $v_t = \omega r$ far from the plate ($z \to \infty$) the radial pressure distribution far from the plate is

$$p(r, z \to \infty) = \frac{\rho\omega^2 r^2}{2} \quad (1.3)$$

This parabolic pressure distribution is consistent with the pressure colour bars shown on Figure 1.6 (You should check that this formula predicts the correct pressure at Point B).

The observed axial pressure gradient is significantly smaller than the radial pressure gradient. This is consistent with the earlier kinematic observation that the axial velocities far above the plate are very small. The small axial pressure gradient is just sufficient to give fluid parcels a weak axial acceleration and to move them upwards away from the plate.

Figure 1.7 illustrates the radial momentum balance between pressure gradient and centrifugal acceleration on a parcel of fluid in the far field region. As the plate is approached, the tangential velocity decreases which
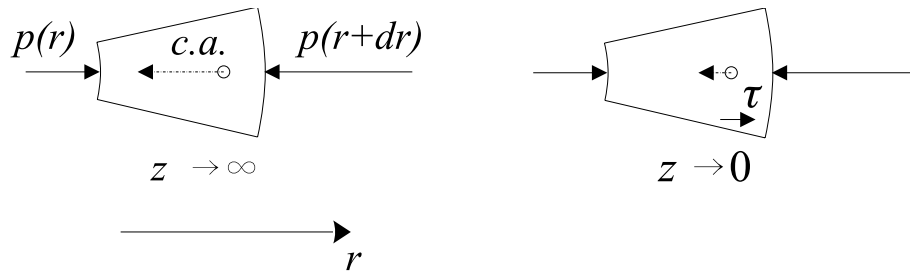
Figure 1.7: Illustration of the radial momentum balance in the far field and near plate regions. Relevant surface pressure forces, centrifugal accelerations (*c.a.*), and net surface shear frictional forces, $\tau$, are shown.

reduces the magnitude of the radial centrifugal acceleration. Since the radial pressure gradient does not change significantly with axial position, an imbalance between the radial pressure gradient and the centrifugal acceleration exists, as shown in the right hand sketch of Figure 1.7. The radial pressure gradient in the near wall region drives fluid in the radial direction towards the axis of rotation and the frictional force in the radial direction created by this flow restores the radial momentum balance.

## 1.3    Model Flow 2

### 1.3.1    Description of Flow Conditions

Figure 1.8 shows the geometry and layout of the second model flow: flow in a cylindrical container with a spinning lid. The container has a radius of $0.025$[m] and a height of $0.025$[m]. The lid of the container is spinning with a rotation rate of $\omega = 0.64[rad\ s^{-1}]$. The fluid in the container is water with nominal STP properties: $\rho = 1000[kg\ m^{-3}]$ and $\mu = 1. \times 10^{-3}[kg\ m^{-1}s^{-1}]$ and it completely fills the container. The rotation rate was set so that the Reynolds number of the flow is $Re \equiv \frac{\rho\omega R^2}{\mu} = 400$. With this low Reynolds number you can expect the flow to be laminar.

The simulated flow field is presented on an uniform mesh with 80 nodes in the axial and radial directions.

### 1.3.2    Exploration

Figure 1.9 shows two views of the velocity field on the $x - z$ meridional plane. The left view shows the axial and radial velocity components on the
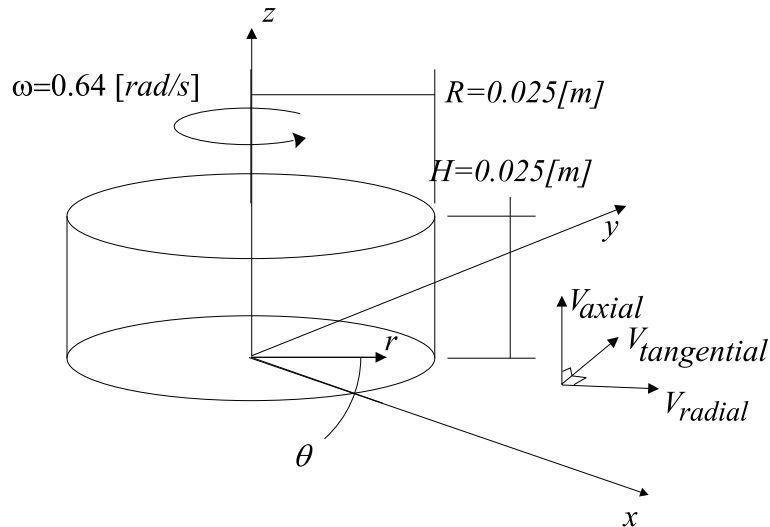
Figure 1.8: Geometry of flow in a container with a spinning lid.

meridional plane while the right view shows all three velocity components on the same plane.

What differences do you notice between this flow field and the infinite flow field without the container walls?

From the right view showing all the three velocity components, you can notice:

- the tangential velocity of the lid varies linearly with radius as expected;

- the speed of the fluid drops rapidly with distance away from the lid. The core of the fluid is rotating much more slowly than the lid; and

- the container wall slows down the fluid in its vicinity significantly.

In the left view, which emphasizes the secondary flow, it is clear that there is single closed cell of fluid rotating in the meridional plane about the point (0.0188[m],0.0[m],0.0183[m])[1].

Figure 1.10 shows a fringe plot of the pressure distribution on the $x - z$ meridional plane. This pressure field is significantly more complex than that of the infinite flow field. What similarities and differences can you notice between this pressure field and that shown in Figure 1.6?

---

[1]These values are in excellent agreement with the benchmark prediction of Lugt and Haussling[11]
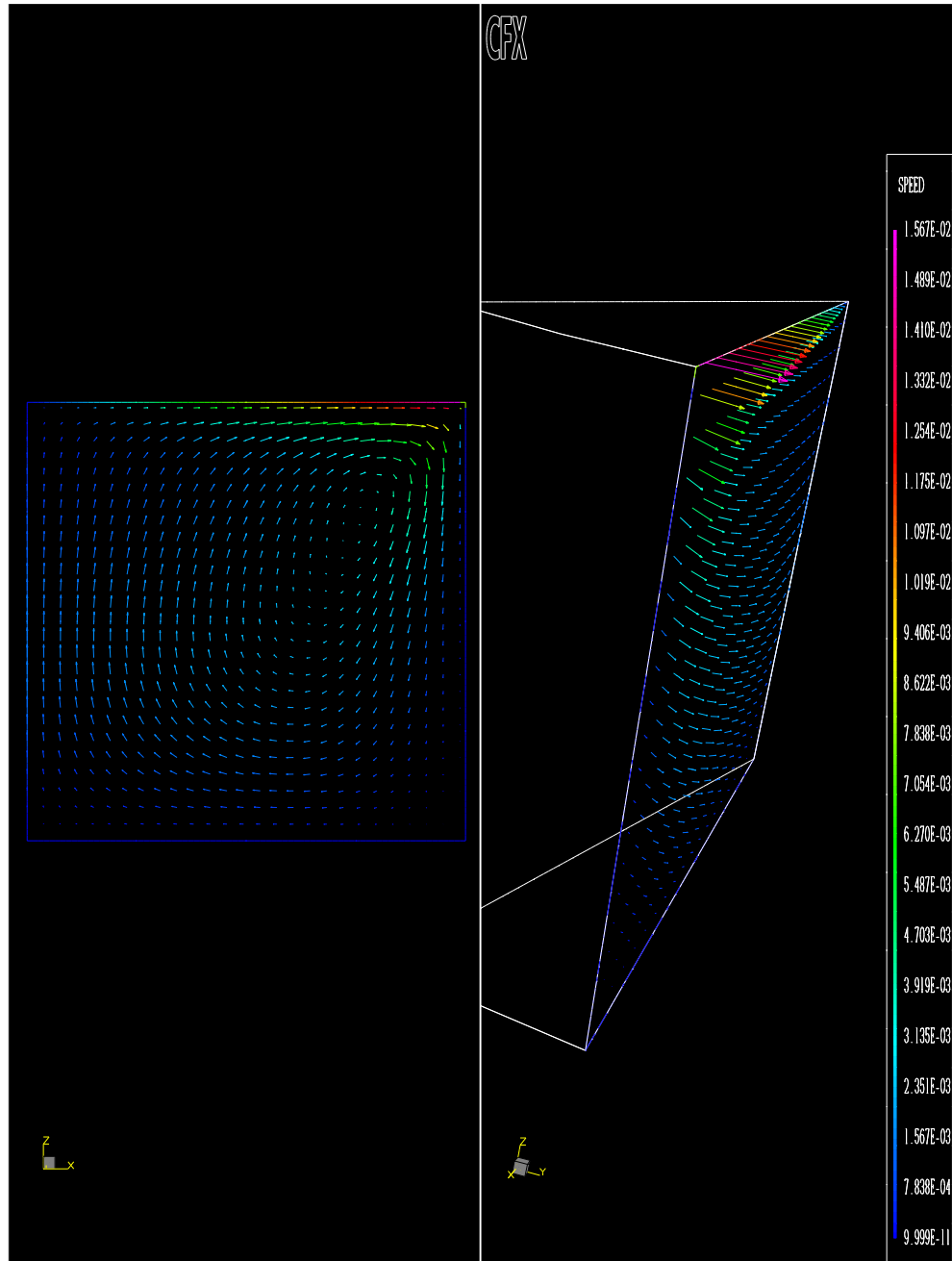
Figure 1.9: Velocity vectors at the nodes on the $x - z$ meridional plane. Right view shows all three vector components and left view shows axial and radial components.
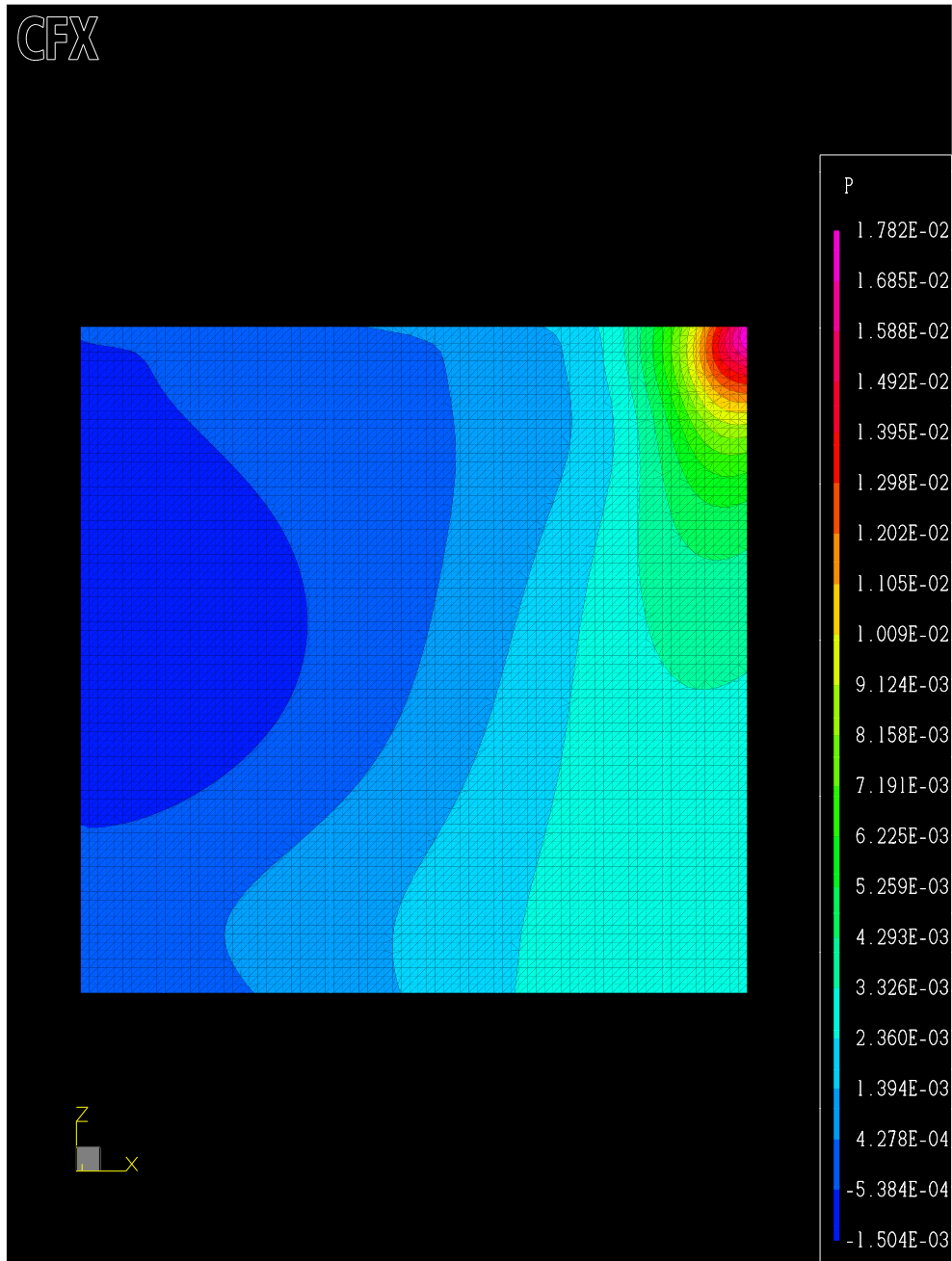
Figure 1.10: Fringe plot of pressure on the on the $x - z$ meridional plane.

The most striking feature of the pressure distribution in the container is the pressure rise near the outer top corner. Some of this pressure rise is partially due to an artiface of the numerical simulation which assumes that there is no gap between the spinning lid and fixed container wall. However, a portion of the pressure rise in the radial direction along the lid balances the centrifugal acceleration of the fluid near the lid. Since the core of fluid near the spinning lid is spinning at a much lower rate than the lid, the pressure in the top corner, $1.8 \times 10^{-2}[Pa]$ is considerably less than that predicted by Equation 1.3, $0.128[Pa]$. Because the radial pressure gradient is less than that required to balance the centrifugal acceleration at the lid, a flow from the axis of rotation to the outer wall is created along the lid as illustrated in Figure 1.11.
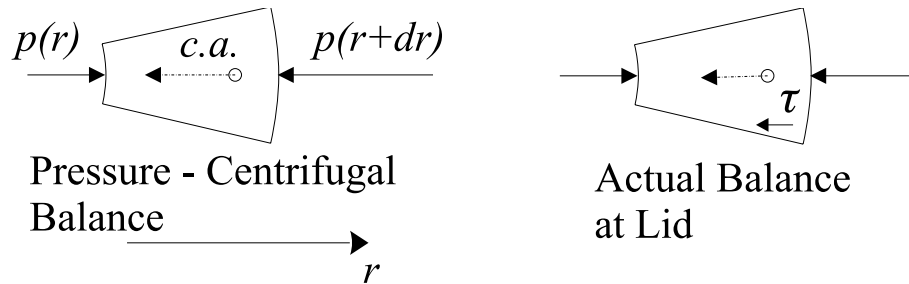


Figure 1.11: Illustration of the radial momentum balance in an ideal pressure gradient/ centrifugal acceleration balance and in the actual balance near the lid. Relevant surface pressure forces, centrifugal accelerations ($c.a.$), and net surface shear frictional forces, $\tau$, are shown.

Between the top of container wall and the container bottom there is a considerable pressure drop. This axial pressure gradient is required to drive the fluid from the top to the bottom in the closed circulation cell and to overcome the viscous drag along the container wall.

Even though there is a significant reduction of the radial pressure gradient between the top and the bottom of the container, the positive radial pressure gradient on the container bottom drives fluid from the container wall to the axis of rotation. The radial momentum balance in the near bottom region is a balance between the radial pressure gradient and the net viscous shear forces resisting motion in the radial direction.

There is a weak negative axial pressure gradient near the axis of rotation to drive the fluid up from the bottom and towards the top of the container.

## 1.4   Further Exploration

In the previous two sections, two model flows have been explored in which a secondary flow pattern is established by the imbalance between radial pressure gradients and centrifugal accelerations. If either model flow were seeded with particles slightly heavier than water then these particles would collect at the bottom near the axis of rotation just as the tea leaves did in the beaker of stirred water.

You can look for similar secondary flow patterns in any situation where the flow is rotating. Common examples include flows in centrifugal pumps, in radial flow turbines, in duct and pipe bends, near car brake disks and near high and low pressure systems in the atmosphere.

Secondary flows can be created by other mechanisms also. For example, secondary flows such as the earth's large scale atmospheric circulation are created by buoyancy forces resulting from temperature variations in the flow field. Another subtle example is the secondary flow in rectangular ducts that is driven by an imbalance in the turbulent stresses.

Even if you do not begin to study secondary flows due to other mechanisms, there is still a lot to be learned about secondary flows in rotating flows. The following questions and suggestions can help you explore this complex subject in further detail:

1. The flow in the beaker has a free surface between the water and the air. Explain the shape of the water surface that is observed;

2. Explain why clear weather is associated with high pressure systems and cloudy weather is associated with low pressure systems;

3. Model Flow 3 is a model flow that is similar to Model Flow 1. In this model flow, the fluid far away from the plate is at rest and the plate is spinning. Before exploring the simulated flow field, see if you can estimate the pressure distribution and directions of the axial and radial velocity components. What similarities are there between this model flow and Model Flow 2 presented above?

4. Model Flow 3 can be simulated with CFD codes. You will have to take care in modeling the boundary condition for the top (far field from the plate). A specified total pressure and flow direction is recommended for this inflow boundary. Why is it adequate to set a zero static pressure condition for the outflow at the outside ($R$) of the domain?

5. Model Flow 4 is laminar flow in a container with a slightly higher Reynolds number, $Re = 1492$, and aspect ratio, $H/R = 1.5$. In what significant way is this flow field dissimilar from that of Model Flow 2 ($Re = 400$)? This flow shows a *vortex breakdown*;

6. Model Flow 5 is a turbulent flow in a container with a spinning lid, $H/R = 1.5$ and $Re = 2.5 \times 10^5$. How does the shape of the turbulent flow field's secondary flow pattern compare to that of Model Flow 4. From this model flow can you see why it is that the tea leaves do not congregate right on the axis of rotation?

7. The torque, $T$, required to turn the spinning lid of the container for Model Flows 2,4, and 5, were estimated from CFX-TASCflow simulations to be $2.06 \times 10^{-7}[N\ m]$, $1.35 \times 10^{-6}[N\ m]$, and $3.36 \times 10^{-3}[N\ m]$, respectively. Schlichting[16] provides the following theoretical correlations for the torque coefficient, $C_T \equiv \frac{2T}{\frac{1}{2}\rho\omega^2 R^5}$, for a spinning plate in an infinite flow:

$$C_T = \begin{cases} \frac{3.87}{Re} & Re < 5 \times 10^4 \\ 0.146Re^{-1/5} & Re > 5 \times 10^4 \end{cases} \qquad (1.4)$$

Plot the predicted torque coefficients and the experimenatal correlations. After noting that the trends of the predicted torque coefficients closely matches thoses of the correlations, provide a list of factors explaining why the predicted values do not exactly agree with the correlations; and

8. Which of the three model flows, 2, 4, or 5, most closely models the flow field that exists in the beaker of stirred water?

### 1.4.1   Annotated Reading List

There is a large literature on centrifugally driven secondary flows and the vortex structures that are created in theses flows. The following texts and articles are recommended for further reading:

**Schlichting[16], pp. 102-107,225-230, and 647-651**  This classic text presents semi-analytical solutions for several laminar flows involing rotation and empirical theories for turbulent flow near spinning disks. The emphasis is on quantitative estimation of measures such as the drag torque on spinning disks,

**Lugt[12], pp.138-145** An excellent description of many flow features of rotating fluids in containers. The use of mathematics is kept to a minimum and the emphasis is on qualitative description,

**Lugt[13], pp.430-435** An updated version of his earlier presentation. This text provides a more complete and mathematical presentation of vortex theory,

**Escudier[7]** A comprehensive summary of the important experiments and theories of the formation and breakdown of vortices in rotating flows,

**Escudier[6]** A well written article showing five examples of flow machinery in which vortices play a significant role in the machine's performance, and

**Daily and Nece[3]** A detailed experimental study of the flow field on the backface of impellers and the resulting frictional losses.

# Chapter 2

# The Extra Shock Wave

## 2.1 The Mystery
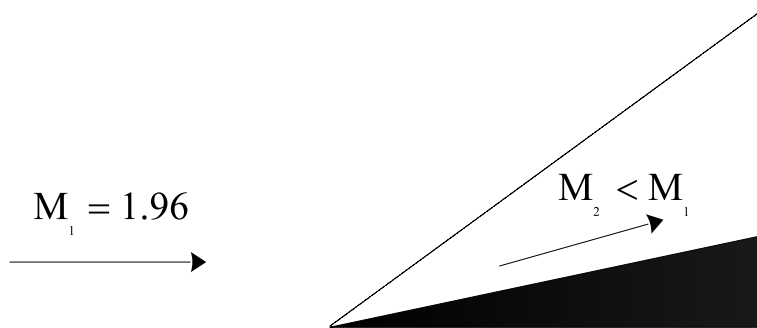


Figure 2.1: Sketch of supersonic flow over the top of a wedge.

One of the features of supersonic flows is that the flow field adjusts suddenly to downstream disturbances. For example, when the flow approaching the two-dimensional wedge show in Figure 2.1 is supersonic there is no physical mechanism for the flow field to adjust to the presence of the wedge before reaching the wedge. Therefore, the flow adjusts by turning suddenly over the oblique shock wave which radiates from the tip of the wedge. Across the shock, the flow angle changes suddenly and there is a corresponding jump in pressure, temperature, and density.

Figure 2.2 is a fringe plot of the relative pressure field for supersonic flow of air over a $10°$ wedge. The oblique shock radiating upwards from the tip of the wedge can be clearly seen. Notice that there is also an oblique shock radiating downwards from the tip even though the bottom surface is parallel
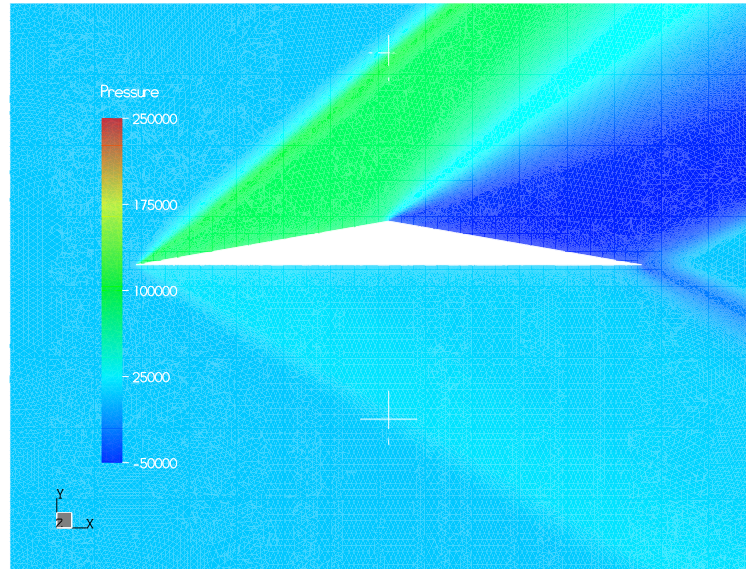
Figure 2.2: Fringe plot of relative pressure $[Pa]$ field for supersonic flow over the a wedge. The reference pressure is $101325[Pa]$.

to the approach flow. What causes this second oblique shock wave?

## 2.2  Model Flows

### 2.2.1  Description of Flow Conditions

The simulation shown in Figure 2.2 is the flow of air at a pressure of $101325[Pa]$ and a temperature of $293.2[K]$ approaching the wedge. The air is travelling at a speed of $673.3[m\ s^{-1}]$ or a Mach number of 1.965 before reaching the tip of the wedge. For the simulations, the air is assumed to be an ideal gas with a constant dynamic viscosity of $1.79 \times 10^{-5}[kg\ m^{-1}s^{-1}]$. Results for two simulations are presented: the first for supersonic flow over a wedge with no-slip boundaries and the second for supersonic flow over a wedge with free slip boundaries. The latter simulates inviscid flow over the wedge.

The wedge has a total length of $2[mm]$ and angles of $10$ ° at the front and back tips. It is assumed that there is no heat transfer from the air to the wedge.

### 2.2.2 Exploration

Examine the following set of fringe plots showing the relative pressure[1] , cross-stream ($v$) velocity, and streamwise ($u$) velocity fields in the vicinity of the wedge. For each field variable two fringe plots are provided: the first for flow over no-slip boundaries and the second for flow over free slip boundaries.

On each fringe plot, two reference points are plotted. Above the wedge, a point is shown along the line that radiates at a 40 ° angle from the tip. This angle corresponds to the angle of an oblique shock for inviscid flow (flow of a fluid with negligible viscous effects) turning through 10°. Below the wedge, a point is shown along the line that radiates at a 31.4° angle from the tip. This angle corresponds to the angle of an oblique shock for inviscid flow turning through 1°.

**Figures 2.3 and 2.4:** From examining the pressure fields notice that:

- there is no shock wave radiating from the lower edge of the tip when the flow is over free slip boundaries,

- the oblique shock angle above the wedge for the flow over the free slip boundaries corresponds very closely to that predicted by the oblique shock relations for inviscid flow,

- the oblique shock angle above the wedge for flow over the no-slip boundaries is greater than that predicted by the oblique shock relations for inviscid flow, and

- the oblique shock below the wedge corresponds closely to an oblique shock of inviscid flow turning through an angle of 1°.

**Figures 2.5 and 2.6:** From examining the cross-stream velocity fields notice that:

- for the flow over the no-slip boundaries, the flow is clearly deflected downwards away from the bottom surface of the wedge,

- the magnitude of the deflection is greatest near the tip of the wedge[2] and then decreases with distance along the bottom surface of the wedge,

---

[1]The relative pressure field is referenced to the approach pressure of $101325[Pa]$. A relative pressure of $0[Pa]$ indicates an undisturbed flow.

[2]The flow angle is 1° downwards near the tip.

- the sudden changes in the flow direction occur over the same areas as the sudden changes in pressure noted in the previous figures (indicating that most flow properties change through the oblique shock wave), and

- the flow does not deflect away from the free slip boundaries.

What causes the flow deflection observed in the cross-stream velocity fringe plots?

**Figures 2.7 and 2.8:** From examining the streamwise velocity fields notice that:

- for the no-slip boundary flows, the fluid adjacent to the boundaries is at rest,

- on these boundaries there is a thin boundary layer of relatively slow moving fluid,

- the boundary layer grows most rapidly near the tip of the wedge, and

- the boundary layer regions are not present when the flow is over the free slip boundaries.
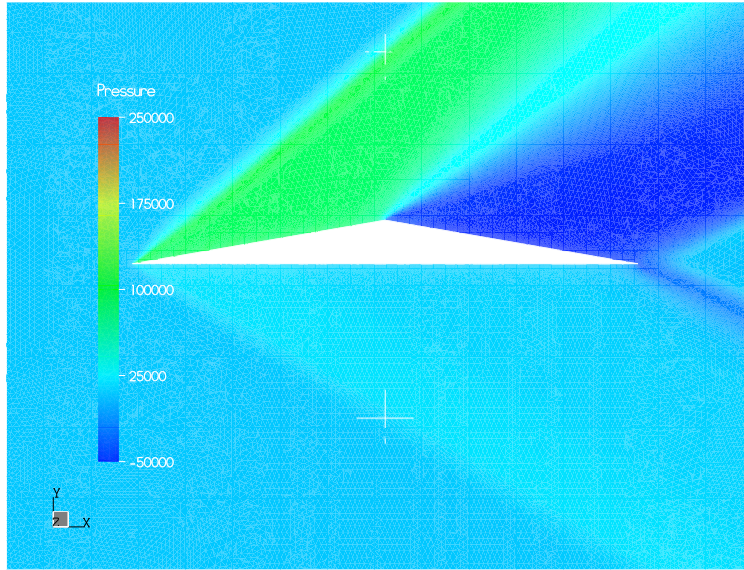
Figure 2.3: Fringe plot of relative pressure $[Pa]$ field for supersonic flow over the a wedge. The reference pressure is $101325[Pa]$.
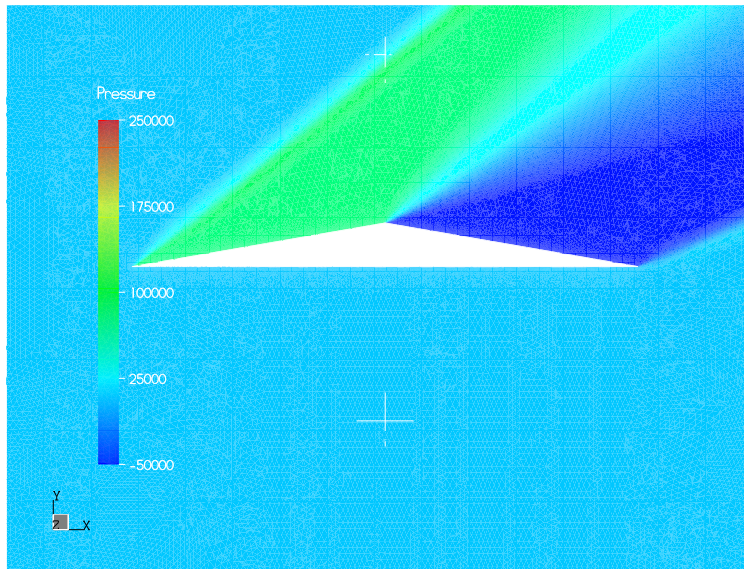


Figure 2.4: Fringe plot of relative pressure $[Pa]$ field for supersonic flow over the a wedge with free slip walls. The reference pressure is $101325[Pa]$.
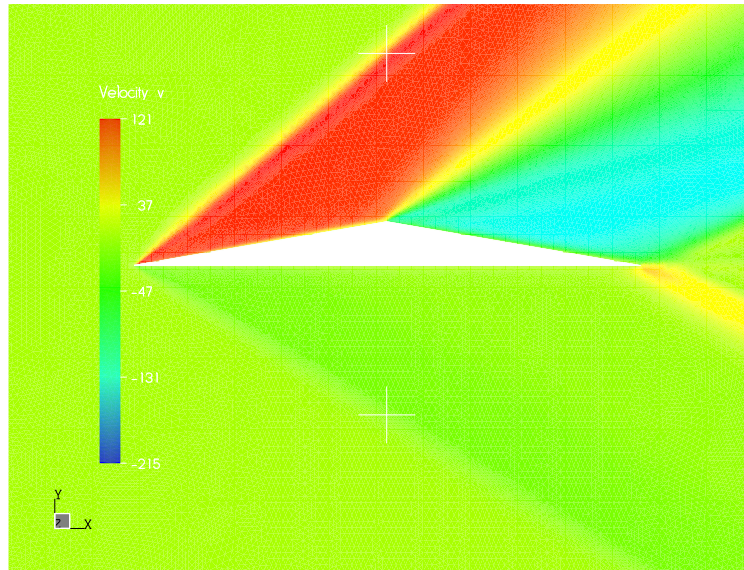
Figure 2.5:  Fringe plot of the cross-stream $(v)$ velocity $[m\ s^{-1}]$ field for supersonic flow over a wedge.
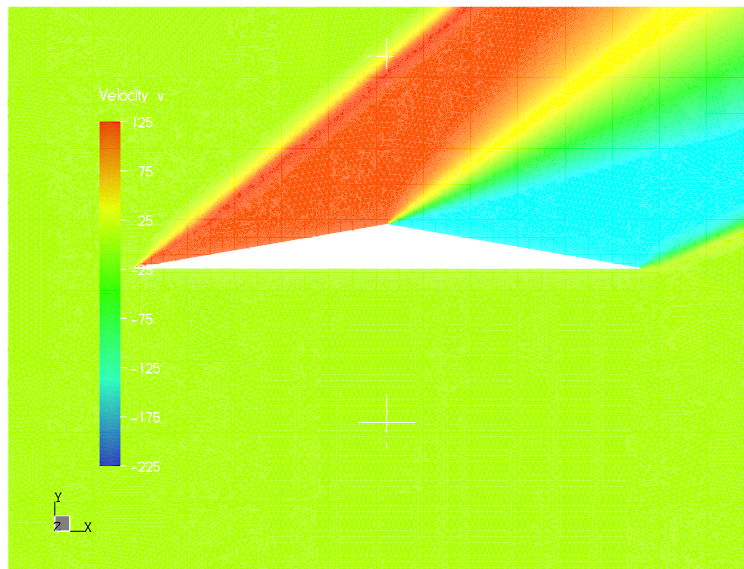


Figure 2.6:  Fringe plot of the cross-stream $(v)$ velocity $[m\ s^{-1}]$ field for supersonic flow over a wedge with free slip walls.
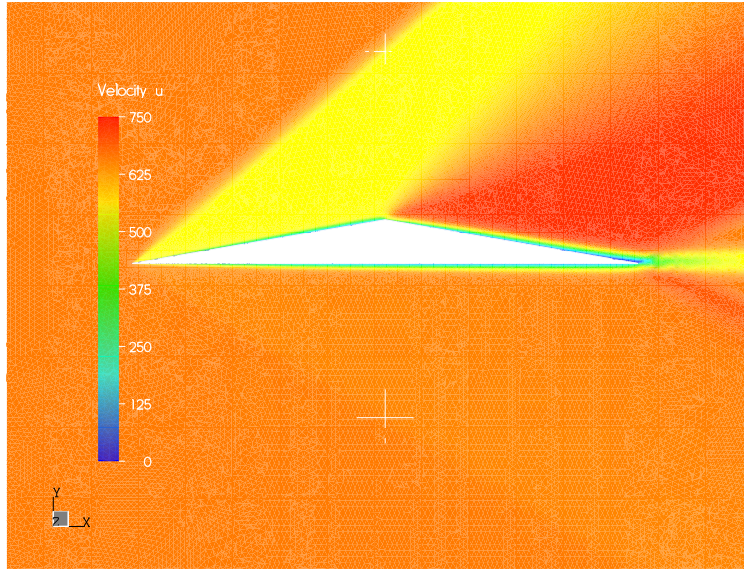
Figure 2.7: Fringe plot of the streamwise $(u)$ velocity $[m\ s^{-1}]$ field for supersonic flow over a wedge.
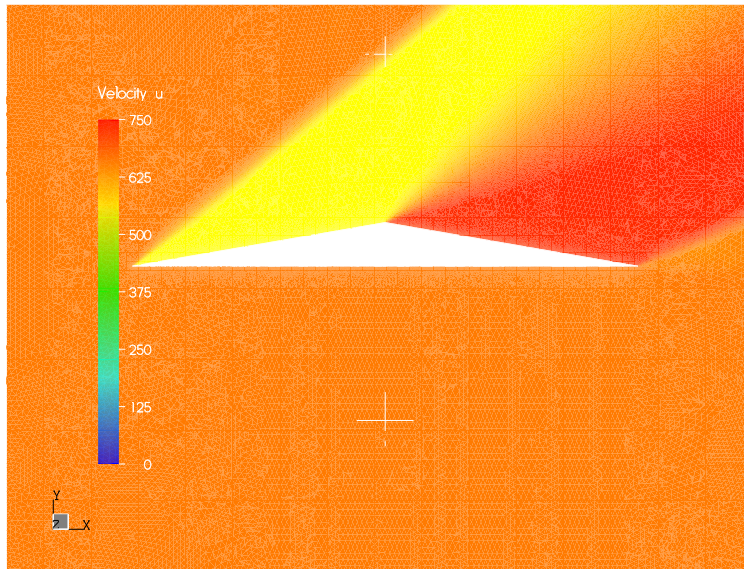


Figure 2.8: Fringe plot of the streamwise $(u)$ velocity $[m\ s^{-1}]$ field for supersonic flow over a wedge with free slip walls.
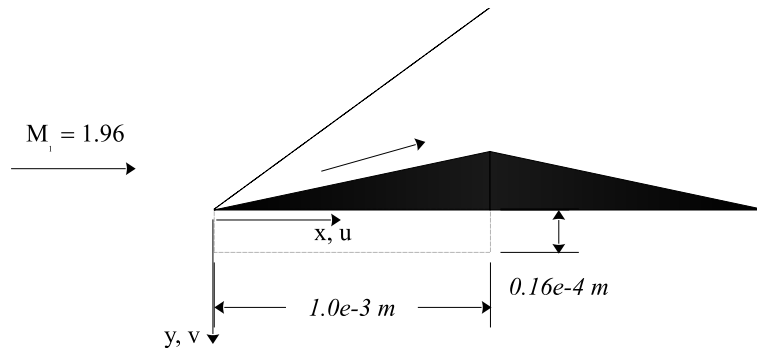
Figure 2.9: Sketch showing the control volume surrounding the boundary layer on the lower boundary of the wedge.

Why does the boundary layer flow generate a cross-stream flow away from the bottom boundary of the wedge?

The above flow field figures show that there are two flow regions for the flow over the wedge with no-slip surfaces: a thin boundary layer region with appreciable shear strain rates and corresponding shear stresses and an external flow region with relatively small gradients except over shock waves. The boundary layer flow region is not present in the flow over the wedge with slip surfaces.

Figure 2.9 shows a control volume that encloses the boundary layer region over the span of $1.0 \times 10^{-3}[m]$ along the lower surface of the wedge. The streamwise, $u$, velocity component carries mass into this control volume across the left face and out of the control volume across the right face. Figure 2.10 shows the the mass flux, $\rho u$, profiles across the left and right faces. It is clear that the total mass flow across the left face:

$$\text{Total Mass Flow} = \int_0^\delta \rho u dy \qquad (2.1)$$

exceeds that across the right face by a significant amount. Since no mass flows across the solid boundary, there must be a cross-stream mass flow away from the boundary layer.

The cross-stream mass flow pushes or displaces the freestream or external flow away from the bottom surface of the wedge. It is this displacement effect that causes the external flow over the no-slip boundary to turn 1° away from the wedge. The turning occurs across the weak oblique shock wave radiating downwards from the tip. As the boundary growth decreases with distance along the surface, the flow angle decreases, as can be seen in Figure 2.5.
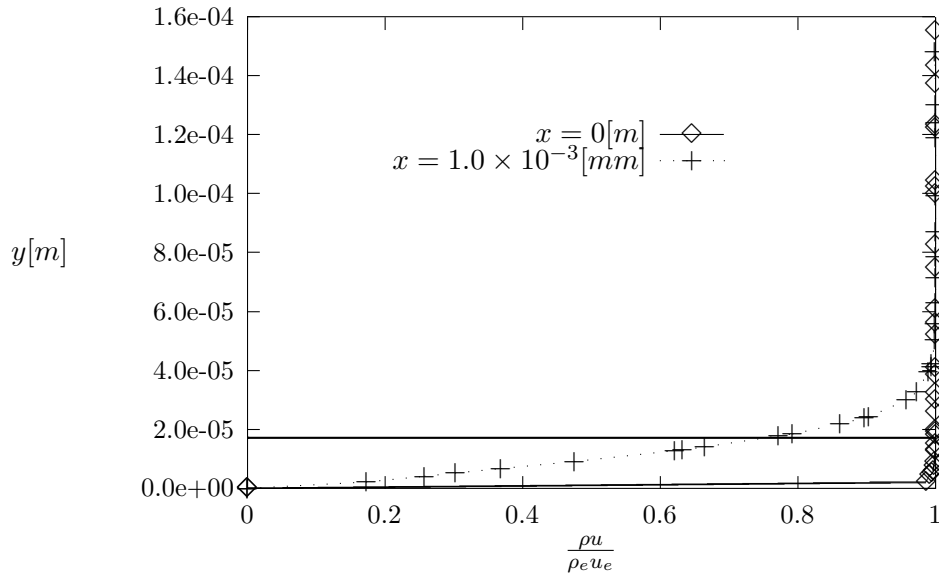
Figure 2.10: Mass flux, $\rho u$, profiles near the lower boundary of the wedge for $x = 0[m]$ and $x = 1.0 \times 10^{-3}[m]$ distances from the tip. The mass flux is normalized by the external flow mass flux, $\rho_e u_e$.

A boundary layer grows on the top surface of the wedge also. This boundary layer causes a displacement effect on the top surface of the wedge. The turning of the external flow that occurs across the top shock must be sufficient to turn the flow away from the solid surface plus the displacement effect. This explains why the oblique shock angle shown in Figure 2.3 is greater than that predicted by the inviscid flow shock relations. While not shown, the oblique shock angle of $41.75°$ in the flow over the no-slip upper surface corresponds to a flow turning angle of $11.5°$ which is the flow angle at the outside of the upper surface boundary layer near the wedge tip.

## 2.3  Further Exploration

The supersonic flow over the wedge, discussed above, illustrates one important consequence of the no-slip condition at solid walls: the boundary displacement effect. This effect is quantified along the length of a developing

boundary layer by the displacement thickness:

$$\delta_1(x) \equiv \int_0^\infty \left(1 - \frac{\rho(x,y)u(x,y)}{\rho_e(x)u_e(x)}\right) dy \tag{2.2}$$

where $x$ is distance along the surface, $y$ is the distance normal to the surface into the flow, and $\rho_e$ and $u_e$ are the local external density and streamwise velocity, respectively. The displacement thickness is the distance that the actual surface appears to be displaced to account for the decrease in the streamwise mass flow in the boundary layer. The displacement thickness $(1.71 \times 10^{-5}[m])$ for the mass flux profile at $x = 1.0 \times 10^{-3}[m]$ on the wedge's lower surface is shown in Figure 2.10 as a dashed line.

The displacement effect is present in both incompressible and compressible flows over streamlined bodies. Engineers designing high efficiency low-drag bodies routinely account for the displacement thickness in their designs. The most recent generations of airfoils for hobby and commercial aircraft, airfoils for wind turbines, and racing car bodies have been designed so that the apparent displaced boundary creates the desired external flow field characteristics, [4].

There are various paths that you can follow for further explorations of these and similar flows:

1. The calculations for the wedge were carried out with a constant viscosity fluid model in order to simplify the discussion. The Excel spreadsheet, Profiles.xls, has the data for two boundary profiles on the lower surface $1.0 \times 10^{-3}[m]$ back from the tip. One set of data is for the constant viscosity model presented above and the other set is for a variable viscosity model:

$$\mu(T) = \mu_0 \left(\frac{T}{T_0}\right)^{\frac{3}{2}} \frac{T_0 + 110[K]}{T + 110[K]} \tag{2.3}$$

   By comparing the data explain why a variable viscosity model is required for a precise simulation of this flow.

2. The results of the previous section shows that supersonic flow deacceleration and compression occurs over very thin thickness of oblique shock waves. Supersonic flow acceleration and expansion occurs over a finite region of Prandtl-Meyer waves. Identify regions of flow expansion in the supersonic flow over the wedge with no-slip surfaces presented in the previous section. Which of these regions is caused, directly or indirectly, by viscous effects?

3. Drag on airfoils and other streamlined bodies is caused both by viscous shear action and net pressure forces. The latter is often referred to as form drag. Estimate the form drag on the wedges with no-slip and slip surfaces. Explain the difference in the two estimates.

### 2.3.1 Annotated Reading List

There is a large literature on boundary layer displacement effects is incompressible and compressible flows. The following are recommended for further reading:

**Van Dyke[20] Photograph 228 page 138** This mystery was inspired by photograph shown below, Figure 2.11, which was taken from Professor Van Dyke's wonderful collection of flow visualization pictures. He suggests that the wedge in the photograph has an angle of 10° and that the bottom surface is parallel to the approach flow. However, the actual experimental conditions as reported by Bardsley and Mair [1] were for a wedge angle of 10.1° and the bottom surface turned 0.3° into the flow. In other words, in this photograph the shock radiating downwards is caused by the turning of the bottom surface and the boundary layer displacement effect. It is reassuring to note that the
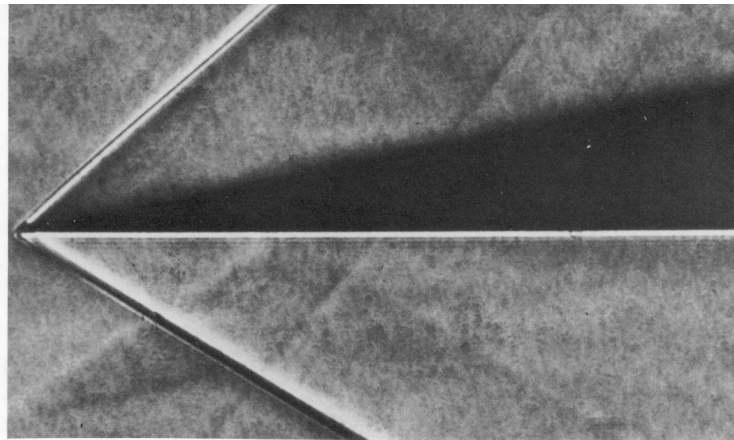


Figure 2.11: Schlieren photograph of air at Mach number =1.965 over a sharp 10.1° wedge. The lower surface is tilted downwards at a slight angle of 0.3°. Scan of the photograph presented by Van Dyke[20]. Original photographs and measurements were made by Bardsley and Mair[1].

upper shock angle of 41.8° predicted in the simulations of the previous section is within the range, $40.3° - 42.3°$, of upper shock angle that can be inferred from the measurements of Bardsley and Mair.

**Eppler**[4]  This text covers the design philosophy and calculation techniques used to design the high-lift and low drag subsonic airfoils in the 1980's and 1990's. The role of the displacement effect and the direct and indirect impact of viscous effects are discussed in detail.

**White**[21] **Chapter 7**  Professor White provides a modern perspective on the physics of compressible boundary layers. The impact of temperature variations on the flow field properties in boundary layers is covered.

# Chapter 3

# The Corner Attraction

## 3.1 The Mystery
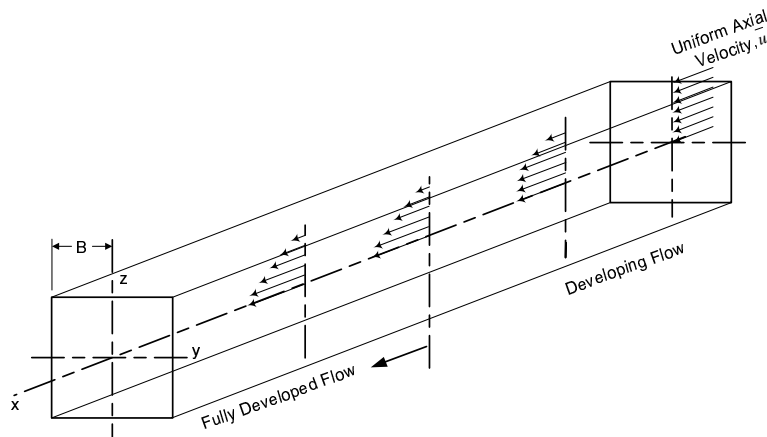


Figure 3.1: Wireframe model of a square duct illustrating the development of the velocity profile on the $y = 0$ centre-plane.

The above figure, Figure 3.1, shows a wireframe model of a long square duct. The $x$ axis, aligned with the duct centre-line, is in the axial direction. If fluid enters the duct with a uniform axial velocity, $\bar{u}$, there will be a region of developing flow in which the shape of the axial velocity profile over the duct cross-sectional area changes with axial distance. Sufficiently far downstream, the flow becomes fully developed. The axial velocity profile no longer varies with axial distance once the flow is fully developed. The fully-developed axial velocity profile, $u(y, z)$, varies, over the duct cross-section,
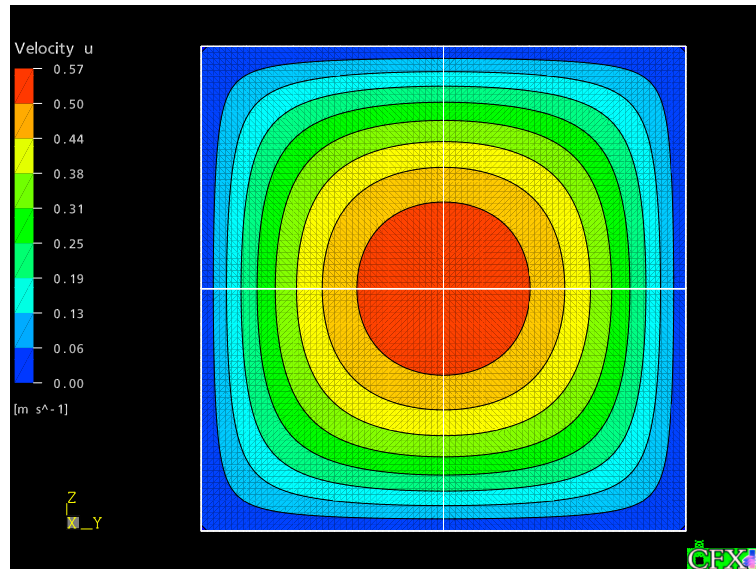
Figure 3.2: Fringe plot of the fully-developed velocity profile of laminar flow through a square duct. The flow direction is out of the page.

from zero at the walls to a maximum at the duct centreline, $(y = 0, z = 0)$.

Figure 3.2 shows the fully-developed velocity profile for incompressible laminar flow through the square duct. Notice how the isovel contours quickly become rounded in the corners. In the vicinity of the upper right corner, the wall shear stresses on the right and top walls act to create a region of relatively slow moving fluid in the corner. For a given distance off the right wall, the axial speed is greater near the $y = 0$ centre-plane than near the corner.

Figure 3.3 shows the fully-developed velocity profile for turbulent flow in the square duct. A difference between the laminar and turbulent profiles is that the rounding of the iso-vel contours in the corners is considerably reduced. Indeed, for a given distance off the right wall, the axial speed increases slightly as the corner is approached from the $y = 0$ centre-plane. It appears that high speed fluid in the core of the duct is being pushed into the corners. Why?
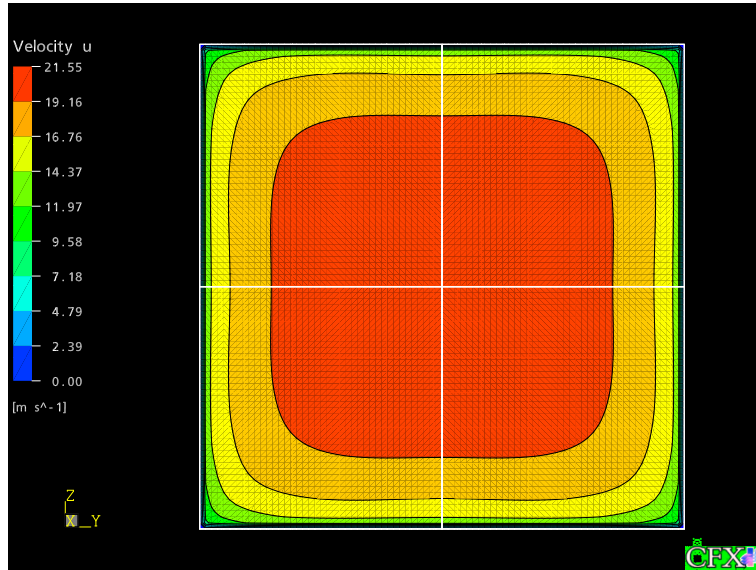
Figure 3.3: Fringe plot of the fully developed velocity profile of turbulent flow through a square duct.

## 3.2  Model Flows

### 3.2.1  Description of Flow Conditions

The simulations presented in the previous section are for the flow of STP (Standard Temperature and Pressure) air through a square duct with a half-width $B = 0.025[m]$. For all simulations, the air is an incompressible gas with density of $\rho = 1.284[kg/m^3]$ and dynamic viscosity of $\mu = 1.725 \times 10^{-5}[kg\ m^{-1}s^{-1}]$. Both laminar and turbulent simulations are presented for the fully-developed flow region. For the laminar flow simulations, the average velocity is $\bar{u} = 0.27[m/s]$ which is equivalent to a duct Reynolds number, $Re_B \equiv \frac{2\rho\bar{u}B}{\mu} \approx 1000$. For the turbulent flow simulations, the average velocity is $18[m/s]$ which is equivalent to a duct Reynolds number of $Re_B \approx 68000$.

In this section more results will be presented for the laminar flow simulation and for two turbulent flow simulations: the first simulation is obtained using an eddy viscosity turbulent kinetic energy - dissipation rate, $k - \varepsilon$ model for the turbulent stresses and the second is obtained using a Reynolds Stress Transport model.

### 3.2.2  Exploration

Examine the set of figures on the following pages that show fringe plots of the axial velocity, the cross-stream velocity vectors, fringe plots of the $x$ component of the vorticity, and fringe plots for the $y$ and $z$ normal friction stress components. For each flow property, three plots are provided: the first for laminar flow, the second for turbulent flow simulated with the $k - \varepsilon$ model, and the third for turbulent flow simulated with a Reynolds Stress Transport model.

**Figure 3.4:** From examining the fringe plots of the axial velocity, $u$, fields notice that:

- For the laminar flow simulation:
  - there is a smooth variation of axial speed over the cross-sectional area. The axial speed is maximum at the duct centre-line ($y = z = 0$) and is zero at the duct walls $y = \pm B$ and $z = \pm B$;
  - the iso-vel contours become rounded near the corners indicating a zone of relatively slow moving fluid in the corner region; and
  - the central iso-vel contours are very close to circular in shape.
- For the turbulent flow simulation obtained with the $k - \varepsilon$ model:
  - there are very large gradients in the axial velocity near the duct walls and the axial velocity is almost uniform over the central portion of the duct (the axial speed is within 11% of the centre-line value over the central 45% of the duct area). The large gradients near the wall are found in other turbulent flows; and
  - the iso-vel contours are again rounded at the corners and the central iso-vel contour is very close to circular in shape.
- For the turbulent flow simulation obtained with the Reynolds Stress Transport model:
  - there are very large gradients in the axial velocity near the wall and the axial velocity is almost uniform over the central portion of the duct; however
  - the iso-vel contours in the centre of the duct are almost square in shape with slightly rounded corners.
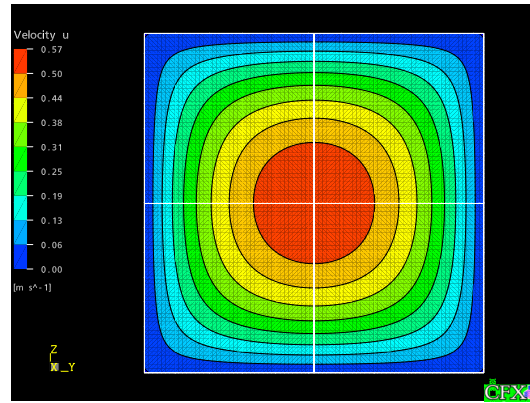
(a) Laminar flow
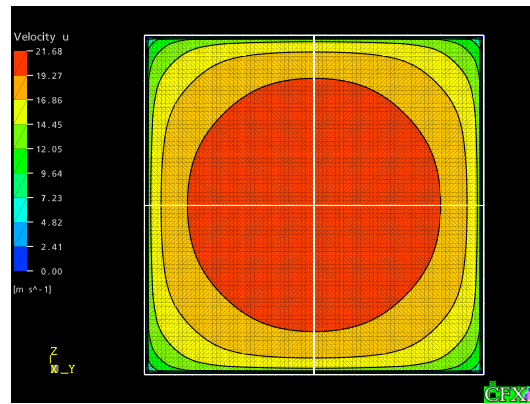


(b) Turbulent flow calculated with $k - \varepsilon$ model
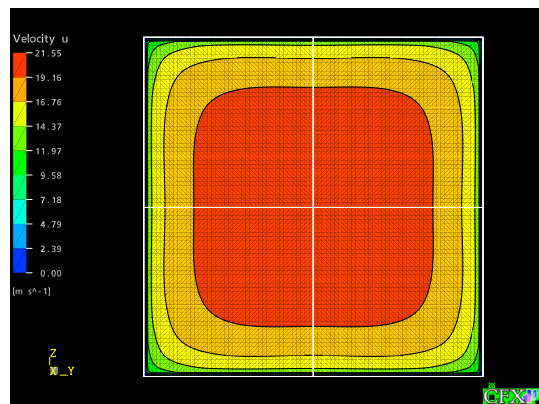


(c) Turbulent flow calculated with Reynolds Stress Transport model

Figure 3.4: Fringe plots of fully developed axial velocity profiles through a square duct.
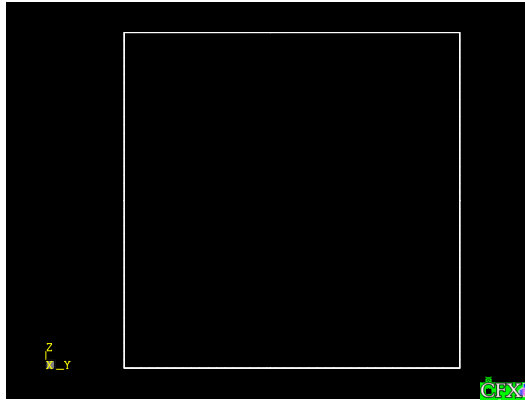
(a) Laminar flow
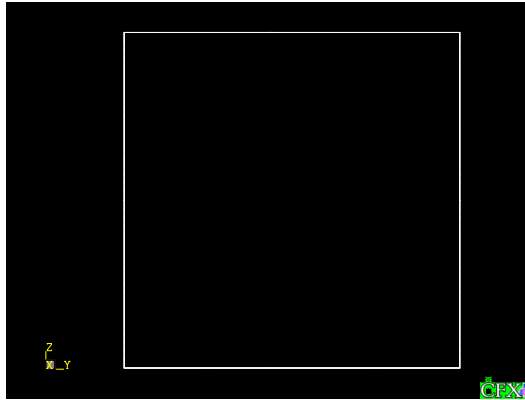


(b) Turbulent flow calculated with $k - \varepsilon$ model
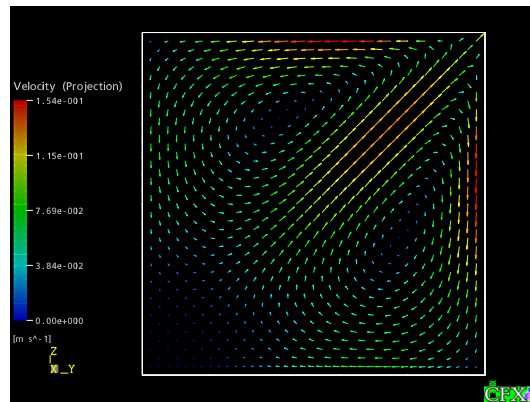


(c) Turbulent flow calculated with Reynolds Stress Transport model

Figure 3.5: Vector plots of cross-stream velocity for fully developed flows in the upper right quadrant of the square duct.
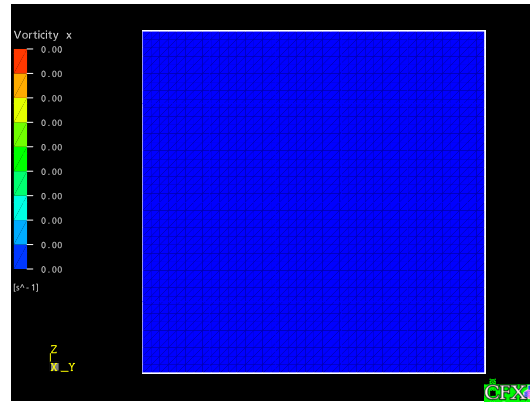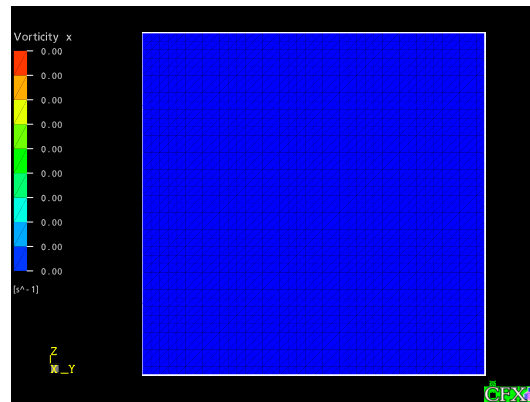
(a) Laminar flow



(b) Turbulent flow calculated with $k - \varepsilon$ model
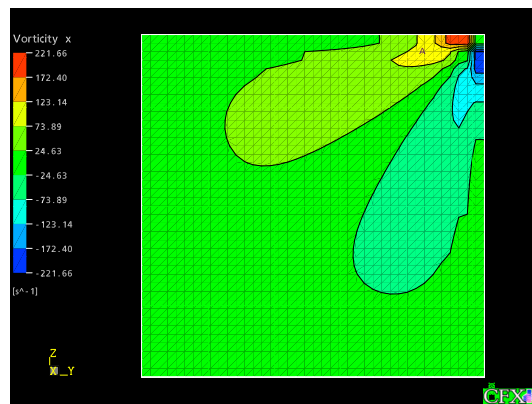


(c) Turbulent flow calculated with Reynolds Stress Transport model

Figure 3.6: Fringe plots of $x$ vorticity component for fully developed flows in the upper right quadrant of the square duct.
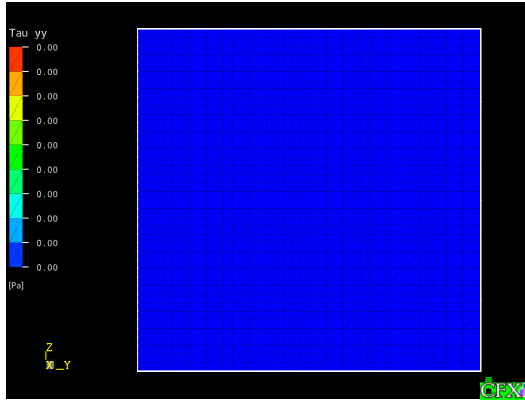
(a) Laminar flow
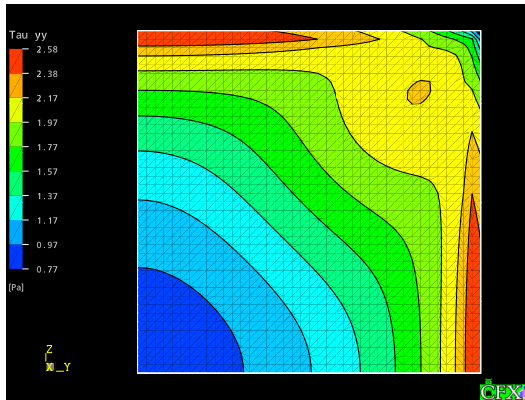


(b) Turbulent flow calculated with $k - \varepsilon$ model
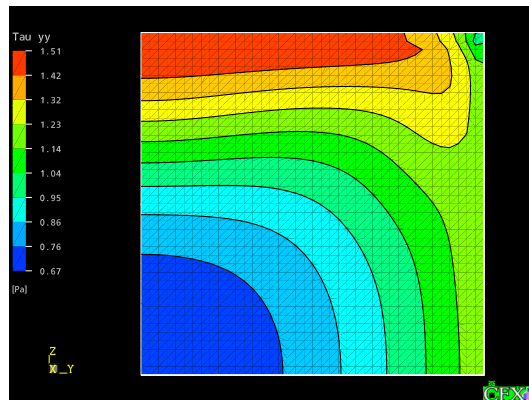


(c) Turbulent flow calculated with Reynolds Stress Transport model

Figure 3.7: Fringe plots of the $y$ normal stress component for fully developed flows in the upper right quadrant of the square duct.
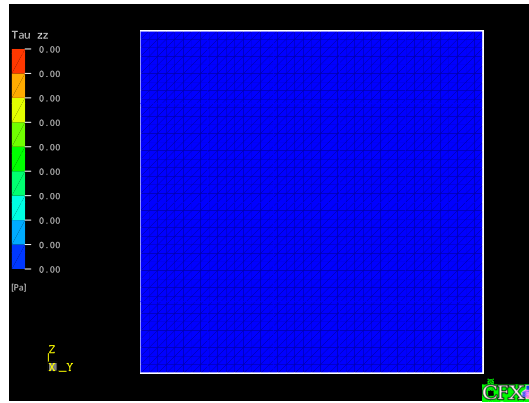
(a) Laminar flow
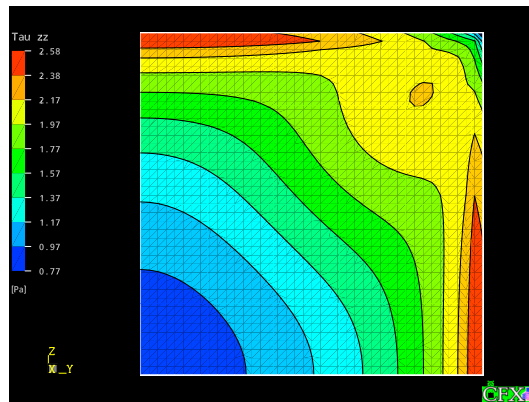


(b) Turbulent flow calculated with $k - \varepsilon$ model
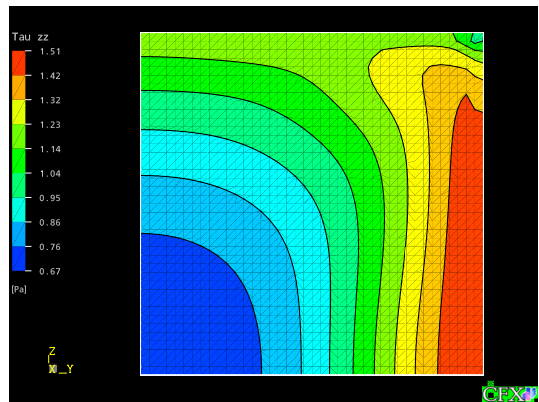


(c) Turbulent flow calculated with Reynolds Stress Transport model

Figure 3.8: Fringe plots of the $z$ normal stress component for fully developed flows in the upper right quadrant of the square duct.

**Figure 3.5:** The cross-stream velocity is defined as $\vec{V}_{c-s} \equiv v\hat{j} + w\hat{k}$ where $v$ and $w$ are the velocity components in the $y$ and $z$ directions, respectively, and $\hat{j}$ and $\hat{k}$ are the unit vectors in the $y$ and $z$ directions, respectively. From examining the cross-stream velocity vector plots notice that:

- For the laminar and the turbulent flow simulation obtained with the $k - \varepsilon$ model there is no cross-stream flow, $v = w = 0$. The axial velocity component is the only component in these flows.

- For the turbulent flow simulation obtained with the Reynolds Stress Transport model there is a cross-stream flow with:
    - two vortex flows in each quadrant of the square duct;
    - in each quadrant, the vortex flow is symmetrical about the radial line running from the duct centre-line to the corner;
    - the flow along the radial symmetry line is from the duct centre-line towards the corner;
    - the centre of the lower vortex is at the non-dimensional location $\frac{y}{B} = 0.76$, $\frac{z}{B} = 0.41$; and
    - the strength of the simulated secondary flow is weak. The maximum speed of the cross-stream velocity, $\vec{V}_{c-s}$, is 0.7% of the centre-line axial velocity.

**Figure 3.6:** From examining the fringe plots of the $x$ component of the vorticity or the cross-stream vorticity, $\zeta_x \equiv \left( \frac{\partial w}{\partial y} - \frac{\partial v}{\partial z} \right)$, notice that:

- the cross-stream vorticity or local fluid rotation velocity is only present in the turbulent flow simulated with Reynolds Stress Transport model;

- The cross-stream vorticity is anti-symmetrical about the radial symmetry line in each quadrant of the square duct; and

- the position of greatest cross-stream vorticity is on the upper wall and in from the corner a distance of 5% of the duct half-width.

**Figures 3.7 and 3.8:** From examining the fringe plots of the $y$ and $z$ normal friction stress components, $\tau_{yy}$ and $\tau_{zz}$, notice that:

- for the laminar flow simulation there are no normal friction stress components;

- for the turbulent flow simulation obtained with the $k - \varepsilon$ model

- both $\tau_{yy}$ and $\tau_{zz}$ vary from $0.77[Pa]$ at the duct centreline to $2.58[Pa]$ near the duct walls,
- $\tau_{yy}$ and $\tau_{zz}$ stress distributions are symmetrical about the radial symmetry line in each quadrant of the square duct, and
- the normal stress components are also *isotropic* in that $\tau_{yy} = \tau_{zz}$; and

- for the turbulent flow simulation obtained with the Reynolds Stress Transport model
  - $\tau_{yy}$ varies from $0.67[Pa]$ at the duct centreline to $1.51[Pa]$ near the top duct wall,
  - $\tau_{yy}$ is weaker near the right vertical wall than it is near the top wall,
  - $\tau_{zz}$ varies from $0.67[Pa]$ at the duct centreline to $1.51[Pa]$ near the right vertical duct wall,
  - $\tau_{zz}$ is weaker near the top wall than it is near the right vertical wall,
  - the $\tau_{zz}$ distribution in the upper right quadrant is the mirror image of the $\tau_{yy}$ distribution when reflected about the radial symmetry line,
  - the normal stress components are *anisotropic* in that $\tau_{yy} \neq \tau_{zz}$.

The turbulent flow through the square duct has a set of eight weak but significant cross-stream vortices or secondary flows. The secondary flow in each vortex is drawn from the centreline towards the duct corner along the radial symmetry line. The simulations demonstrate that the existence of the secondary flow is connected to the distribution of anisotropic normal stresses, $\tau_{yy}$ and $\tau_{zz}$. How do the anisotropic normal stresses create the secondary flow?

The simplest explanation of the physics of the secondary flow in a square duct was proposed by Speziale[17] and is based on the axial vorticity, $\zeta_x$. The axial vorticity is twice the local counterclockwise (ccw) angular velocity of fluid parcels in the cross-stream or $y - z$ plane. From the definition of the axial vorticity,

$$\zeta_x \equiv \left( \frac{\partial w}{\partial y} - \frac{\partial v}{\partial z} \right) \tag{3.1}$$

it is clear that there will only be axial vorticity if there are velocity components in the cross-stream plane, $v$ and $w$. For the fluid parcels to have
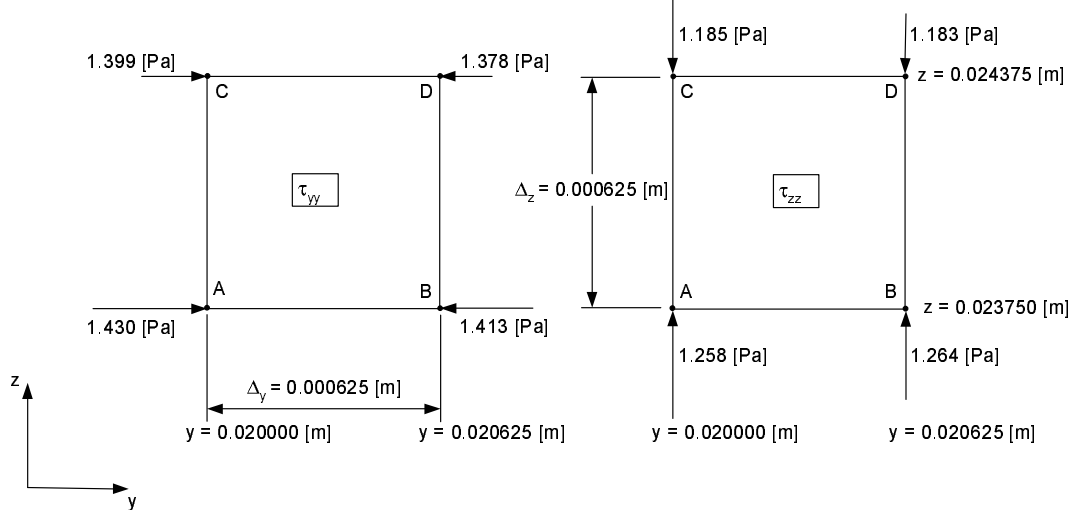
Figure 3.9: Fluid parcel in a region of high axial vorticity near the right wall with normal stresses shown on the parcel corners.

angular velocity in the cross-stream plane there must be a moment in the cross-stream plane to create the spin.

Figure 3.9 shows two views of a small fluid parcel, $\Delta_y = \Delta_z = 0.000625[m]$, located with its lower left corner at $A(y = 0.020[m], z = 0.02375[m])$. As shown in Figure 3.6c, point A lies near the top wall and is in a region of high (ccw) vorticity, $\zeta_x = 80[s^{-1}]$. The left view of the parcel shows the values of the $\tau_{yy}$ normal stress on the four corners of the parcel and their action to create forces and moments on the parcel. The right view shows the corresponding values of the $\tau_{zz}$ normal stress.

Consider the $\tau_{yy}$ normal stresses acting at points **B** and **D**. If $\left.\frac{\partial \tau_{yy}}{\partial z}\right|_{BD} > 0$, or $\tau_{yy}|_D > \tau_{yy}|_B$, then a counterclockwise moment about the parcel's centre is created on face **BD**. However, if $\left.\frac{\partial \tau_{yy}}{\partial z}\right|_{AC} > 0$ then a clockwise moment about the parcel's centre is created on face **AC**. The net strength of the counterclockwise moment on the parcel due to the $\tau_{yy}$ normal stress is proportional to

$$\frac{\partial^2 \tau_{yy}}{\partial y \partial z} \tag{3.2}$$

Similarly, there will be a counterclockwise moment created on face **CD** by the $\tau_{zz}$ normal stresses if $\left.\frac{\partial \tau_{zz}}{\partial y}\right|_{CD} < 0$. This counterclockwise moment

will be offset by a clockwise moment on face **AB** if $\left.\frac{\partial \tau_{zz}}{\partial y}\right|_{AB} < 0$. Therefore the net strength of the counterclockwise moment on the parcel due to the $\tau_{zz}$ normal stress is proportional to

$$-\frac{\partial^2 \tau_{zz}}{\partial y \partial z} \tag{3.3}$$

Combining the above shows that a counterclockwise moment about the parcel's centre is created if

$$\frac{\partial^2}{\partial y \partial z}\left(\tau_{yy} - \tau_{zz}\right) > 0 \tag{3.4}$$

In other words, a secondary flow will exist if:

- the normal stresses are anisotropic, $\tau_{yy} \neq \tau_{zz}$, and

- the stress difference, $\tau_{yy} - \tau_{zz}$, varies in both directions in the cross-stream plane, $y$ and $z$.
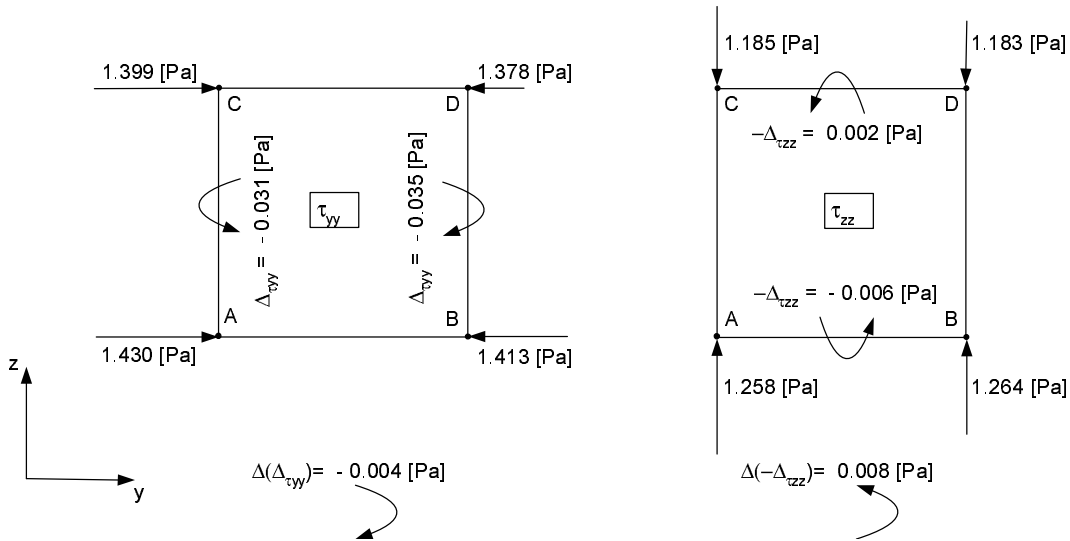


Figure 3.10: Fluid parcel showing the signed normal stress differences on each face.

Figure 3.10 shows the fluid parcel again with the signed normal stress differences on each face along with the moment direction implied by each

stress difference. Applying a finite difference approximation:

$$\frac{\partial^2}{\partial y \partial z} \left(\tau_{yy} - \tau_{zz}\big|_{\text{parcel}} \approx \left(\frac{-0.004[Pa] + 0.008[Pa]}{(6.25 \times 10^{-4}[m])^2}\right) \approx 1.024 \times 10^4 [Pa/m^2]$$

(3.5)

In other words there is a significant positive or counterclockwise moment (per unit volume) acting on the fluid parcel. This moment creates a high counterclockwise angular velocity or positive vorticity in this region.

## 3.3   Further Exploration

The secondary flow set up in the cross-stream plane of the square duct is an example of a type two secondary flow. Type one secondary flows are driven by body forces and include the secondary flow close to a spinning disk discussed in Chapter 1, *The Fate of Sinking Tea Leaves*. Type two secondary flows are driven by normal stresses. For Newtonian fluids, type two secondary flows only exist in turbulent flows.

### 3.3.1   Role of the Turbulence Model

As shown in the original exploration, the simulation of the secondary flow in the square duct is very sensitive to the choice of turbulence model for the turbulent Reynolds stresses. The eddy viscosity $k - \varepsilon$ model failed to predict a secondary flow and the Reynolds stress transport model predicted the secondary flow to reasonable accuracy. In this sub-section the physics of these two turbulence models are briefly reviewed to explain the inadequacy of the eddy viscosity model for this flow. Given the importance of the normal stresses in establishing the vorticity in the cross-stream plane, the focus is on the turbulent normal stress modelling.

The normal stresses, $\tau_{xx}, \tau_{yy}, \tau_{zz}$ are related to the turbulent velocity fluctuations,

$$\tau_{\alpha\alpha} = \rho \overline{u'_\alpha u'_\alpha}$$

(3.6)

where $\alpha$ represents one spatial direction, $x, y$ or $z$, no summation is implied, and $u'_\alpha$ is the turbulent velocity fluctuation in the $\alpha$ direction. The turbulent normal stresses are also related to the turbulent kinetic energy, $k \equiv \frac{\overline{u'u'}}{2} + \frac{\overline{v'v'}}{2} + \frac{\overline{w'w'}}{2}$,

$$\tau_{xx} + \tau_{yy} + \tau_{zz} = 2\rho k$$

(3.7)

The relative sizes of the three normal stresses are determined by how the turbulent kinetic energy is distributed over the three directions.

The eddy viscosity model for the turbulent normal stresses is:

$$\tau_{\alpha\alpha} \approx \frac{2}{3}\rho k - 2\mu_T \frac{\partial u_\alpha}{\partial x_\alpha} \tag{3.8}$$

where $\mu_T$ is the turbulent viscosity (a property of the turbulence). In the fully developed flow through the square duct the streamwise velocity, $u$, is significantly larger then the cross-stream velocity and $\frac{\partial u}{\partial x} \approx 0$. Therefore, eddy viscosity models like the $k - \varepsilon$ model predict that all three normal stress components are identical, $\tau_{\alpha\alpha} = \frac{2}{3}\rho k$. This normal stress isotropy was noted in Figures 3.7 and 3.8.

In Reynolds stress transport models, the transport of the individual stress components is modelled with transport equations of the form:

$$\frac{\partial \tau_{ij}}{\partial t} + C_{ij} = D_{ij} + P_{ij} + \Pi_{ij} - \rho\varepsilon_{ij} \tag{3.9}$$

where $C_{ij}$ is the convective transport of $\tau_{ij} \equiv \rho\overline{u_i' u_j'}$ by the mean flow field, $D_{ij}$ is the diffusive transport of $\tau_{ij}$ by the turbulence field, $P_{ij}$ is the shear production of $\tau_{ij}$ through products of the shear stresses and mean velocity gradients, $\Pi_{ij}$ is the redistribution of the turbulent kinetic energy between the three directions, and $\varepsilon_{ij}$ is the dissipation of $\tau_{ij}$ by molecular action. The convective transport and shear production terms can be represented exactly in terms of the Reynolds stresses and mean flow gradients. Closure models are required for the other three terms.

If the streamwise velocity, $u$, dominates and the flow is fully developed, $\frac{\partial}{\partial x} \approx 0$, then the shear production terms for the three normal stresses are:

$$\begin{aligned}
P_{xx} &= -2\rho\overline{u'v'}\frac{\partial u}{\partial y} - 2\rho\overline{u'w'}\frac{\partial u}{\partial z} & (3.10) \\
P_{yy} &= 0 & (3.11) \\
P_{zz} &= 0 & (3.12)
\end{aligned}$$

This shows that fluctuations in the streamwise direction, $u'$, are produced directly by the mean flow gradients. However, fluctuating velocity components, $v'$ and $w'$, exist in the two cross-stream directions, even though there is no direct production mechanism for these fluctuations.

The $\Pi_{\alpha\alpha}$ redistribution terms are responsible for creating fluctuations in the cross-stream directions. There are two redistribution processes: a slow tendency driven by the random motion of the turbulent flow field to

move towards an isotropic state and a rapid process of cross-stream fluctuation creation to conserve mass in the fluctuating velocity field. The latter is pertinent to the study of anisotropy in the square duct flow. When a streamwise fluctuating component is created at a point in space, there must be cross-stream fluctuating components created to conserve mass:

$$\frac{\partial u'}{\partial x} = -\left(\frac{\partial v'}{\partial y} + \frac{\partial w'}{\partial z}\right) \tag{3.13}$$

In regions far from walls, there will be no bias in the creation of $v'$ and $w'$ fluctuations. For the simulated flow near the centreline of the duct $\tau_{yy} = \tau_{zz} = 0.67[Pa]$ and $\tau_{xx} = 1.37[Pa]$. The streamwise normal stress is the highest because of the direct shear production of $u'$ fluctuations, $P_{xx}$. However, approximately half of the kinetic energy produced by this production is redistributed equally between the $v'$ and $w'$ cross-stream fluctuations.

At a point near the top wall, like point A shown in Figure 3.6c, the presence of the wall will preferentially damp fluctuations in the $z$ direction. In effect, it is easier to pull fluid from the $y$ direction to satisfy the mass imbalance created by a shear produced $u'$ fluctuation then from the $z$ direction because of the blockage by the wall. At point A in the simulated flow, $\tau_{zz} = 1.26[Pa]$, $\tau_{yy} = 1.43[Pa] > \tau_{zz}$, and $\tau_{xx} = 3.11[Pa]$. Again the streamwise normal stress is the greatest but the redistribution between the $v'$ and $w'$ fluctuations is not equal. This is the mechanism that produces the anisotropy in the cross-stream normal stresses that is responsible for creating the secondary flow. An eddy viscosity turbulence model, like the $k - \varepsilon$ model, is not capable of reproducing this anisotropy and therefore cannot reproduce the secondary flow.

### 3.3.2 Impact of Secondary Flow

As shown in the original explorations, the secondary flow has a profound effect on the shape of the streamwise, $u$, velocity contours even though the strength of the cross-stream secondary flow is weak. How important is the secondary flow to the dynamics of the flow through the square duct?

Table 3.1 shows the predicted friction factors from the $k-\varepsilon$ and Reynolds Stress Transport Model (RSTM) simulations. This data shows that the secondary flow does not have any impact on the friction factor. Indeed, the simulated friction factor is very close to that predicted by the Moody diagram for fully developed flow through a round pipe with a hydraulic diameter, $D_h$:

$$D_h \equiv \frac{4\mathcal{A}}{\mathcal{P}} = 2B \tag{3.14}$$

| Geometry | Model | $Re_B$ | $f$ |
|---|---|---|---|
| Square Duct | CFX-5 RSTM | 68,000 | 0.018 |
| Square Duct | CFX-5 $k - \varepsilon$ | 68,000 | 0.018 |
| Round Pipe | Moody Diagram[22] | 68,000 | 0.019 |

Table 3.1: Comparison of the predicted friction factors from the $k - \varepsilon$ and RSTM simulations to the Moody diagram value.

where $\mathcal{A}$ is the cross-sectional area, and $\mathcal{P}$ is the duct perimeter.

The relative insensitivity of the friction factor to the duct geometry and to the presence of the secondary flow is due to two factors:

1. the low speed in the secondary flow vortices, and

2. the strong velocity gradients in the thin *log-law* region adjacent to the duct walls.

All of the preceding discussion has been for fully-developed duct flows. The impact of the secondary flow is more significant in geometries with axial acceleration. For example, in a nozzle with a square cross-sectional area, the axial speed will increase as the flow moves through the nozzle and the axial strain rate, $\frac{\partial u}{\partial x} > 0$, is positive. The secondary vortices created in the corner of the nozzle will be stretched in the axial direction. As the vortices are stretched, their effective diameter will decrease. To conserve angular momentum, the cross-stream (rotational) speed of the vortices will increase (similar to the increase in rotational speed observed when a figure skater draws in their arms).

These dynamics are significant for turbulent flows along corners between two walls. Besides being observed in square ducts, they are also observed in other non-circular duct geometries (i.e. rectangular and triangular ducts) and at the junction of a wing and an aircraft body [10].

Options for more exploration of this complex flow include:

**Law of the Wall:** For many turbulent flows, the streamwise velocity profile near solid walls has the universal functional form:

$$u^+ \equiv \frac{u(x, y)}{u^*} = \text{function}\left(y^+ \equiv \frac{\rho u^* y}{\mu}\right) \qquad (3.15)$$

where $u^* \equiv \sqrt{\tau_w(x)/\rho}$ is the wall shear velocity, $\tau_w(x)$ is the local wall shear stress, and $y$ is distance off the wall. For $y^+ > 30$ the function

has a logarithmic form, [21]. Using the data from the simulation of fully developed flow through a square duct with a Reynolds Stress Transport Model, stored in the spreadsheet SquareDuctData.xls, plot $u^+$ vs $y^+$ on semi-log plots for $z = 0, 0.005, 0.01, 0.015, and 0.02[m]$.

**Normal Stress Anisotropy:** Using the data stored in SquareDuctData.xls calculate the normal stress anisotropy, $\overline{v'v'} - \overline{w'w'}$, over the cross-section of the duct $0 < y, z < 0.025[m]$. Relate these values to the regions of high vorticity shown in Figure 3.6.

**Vortex Production** Pettersson Reif and Andersson [14] show that the secondary flow Reynolds shear stress, $\overline{v'w'}$, plays a significant role in maintaining the secondary flow initially created by normal stress anisotropy. Using the data in SquareDuctData.xls, estimate the variation the secondary vortex production term,

$$\frac{\partial^2 \overline{v'w'}}{\partial z^2} - \frac{\partial^2 \overline{v'w'}}{\partial y^2} \tag{3.16}$$

over the duct cross-sectional area.

### 3.3.3   Annotated Reading List

The secondary turbulent corner flow makes an interesting and subtle test base for understanding the dynamics of turbulent flows. The following is recommended for further reading:

**Johnston[10]** Professor Johnston's article gives a thorough review of the two types of secondary flows. Secondary flows in corners are reviewed for internal duct and external flows.

**White[22] Chapter 6** In this introductory text, Professor White introduces the concept of hydraulic diameter for the modelling of pressure drop in non-circular ducts. There is a brief introduction to secondary flow in the presentation.

**Speziale[17]** This pioneering article discusses the requirements for a model of the turbulent Reynolds stresses to successfully capture the secondary flow pattern in rectangular ducts.

**Huser and Biringen[9]** Presents the findings from an analysis of the complete transient turbulent flow field obtained by direct numerical simulation of the transient Navier-Stokes equations for flow in a square

duct. The transient details of the turbulent eddy motion were resolved in this simulation.

**Pettersson Reif and Andersson[14]** Presents a complete analysis of the dynamics of the flow in a square duct based on a simulation obtained with a Reynolds Stress Transport Model similar to that used in the present work.

# Appendix A

# Sinking Tea Leaf Model Flow Calculations

All model flows were calculated using water with nominal properties:, $\rho = 1000[kg\ m^{-3}]$ and $\mu = 1.0^{-3}[kg\ m^{-1}s^{-1}]$. The outer radius of all containers (and flow domains) was $R = 0.025[m]$.

## A.1   1: Spinning Flow Above an Infinite Plate

The simulated flow field of a rotating fluid above an infinite flat plate were calculated with a semi-analytical procedure. Scale analysis of the full set of momentum equations shows that a the solution can be obtained from a set of non-dimensional ordinary equations. The similarity transformation reduces the radial and axial variation to a variation in a non-dimensional axial coordinate, $\zeta$. The derivation and solution of the similarity equations was first presented by U.T. Boedewadt and is reproduced (with corrections) in Schlichting [16].

A finite volume numerical solution technique was developed for solving the similarity equations and was implemented in Matlab 6.0. Full details of the derivation of the solution technique are given in a separate report, Stubley [19]. Three Matlab 6.0 script files are available for computing and visualizing the flow field:

**makeprofile.m** code to calculate the finite volume solution of the non-dimensional similarity profile functions on a fine mesh. The results are written out to a Matlab data file, `profile.mat` for use in post-processing;

**export2tascflow.m** code to transform the non-dimensional profile functions into dimensional velocity and pressure fields in Cartesian coordinates. The results are interpolated onto a CFX-TASCflow mesh and exported in an `rsf` file for visualization processing inside CFX-TASCflow. Note that indirect flow field properties like shear strain rates, stresses, streamlines, etc. are not available; and

**plotstreak.m** code to transform the non-dimensional profile functions into dimensional velocity and pressure fields in Cartesian coordinates. The solution is interpolated onto the coarse mesh and a set of streaklines are calculated. The resulting plot is animated.

A set of CFX-TASCflow files are also available for visualizing the flow field:

**grd** the grid file for a structured mesh of nodes in the $x - z$ plane. Twenty one nodes are placed in the axial direction ($H = 0.01[m]$) and eleven nodes are placed in the radial direction, ($R = 0.025[m]$). For the brave of heart, a set of files, `gdf, cdf, sdf`, and `idf`, are included for generating this mesh with CFX-TASCGrid;

**name.lun** the CFX-TASCflow system control file;

**prm** a minimal CFX-TASCflow parameter file;

**rso** a minimal CFX-TASCflow field data file;

**viz.state** the information to create the images used in this study; and

**rsf** the fine grid Matlab 6.0 velocity and pressure field solution interpolated onto the CFX-TASCflow grid. To use this information restore the post-processing state with `viz.state` and then use the Command Line Tool to execute the command:"`read rsf`".

You may wonder why CFX-TASCflow (or another commercial CFD package) was not used to generate the simulated flow field for this model flow. The boundary conditions for the wall, axis of rotation and far field top are all easily modeled. The boundary condition for the outer cylindrical surface is the challenge. The velocity profile over this surface involves regions of both inflow and outflow and this profile is inherently part of the solution. A well-posed CFD problem requires that the flow field properties be uniquely specified at all inflow regions and that is not possible for this flow. The semi-analytic solution avoids this problem by analytically accounting for the radial variation and therefore does not require a boundary condition for this surface.

## A.2   2: Flow in a Container with a Spinning Lid

A full set of CFX-TASCflow files are provided for this model flow. The mesh is generated with CFX-TASCGrid and is made up three meridional planes. The outer two meridional planes define a wedge with an included angle of 20°. A relatively fine mesh with 80 nodes in the axial and radial directions is used for each meridional plane.

The calculations were done in a rotating reference frame with zero rotation rate (this ensures access to post-processing features for rotating flows). The alternate numerics parameter for rotating reference frames was chosen to ensure accurate discretization as fluid parcels travel into regions of varying bulk rotation about the centre line axis. Water with nominal STP properties, $\rho = 1000[kg\ m^{-3}]$ and $\mu = 1. \times 10^{-3}[kg\ m^{-1}s^{-1}]$ was the working fluid.

The axis of rotation was modeled as a symmetry line. The bottom and side/outer wall of the container were fixed walls and the lid was a wall boundary with a rotation rate of $\omega = 0.64[rad\ s^{-1}]$.

A second order accurate Linear Profile Skew scheme with Physical Advection Correction (PAC) was used to discretize the advective fluxes. A time step of $5[s]$ was used to obtain a steady state solution with the maximum residual below $1.0 \times 10^{-5}$.

A macro, *torque*, is included in the [gci] file for calculating the torque, $T[N\ m]$, required to turn the spinning lid of the container.

## A.3   3: Flow above an Infinite Spinning Plate

MatLab and CFX-TASCflow files similar to those for Model Flow 1 are provided.

## A.4   4: Vortex Breakdown Flow in a Container

The CFX-TASCflow set up for this model flow was identical to that of Model Flow 2 except that the rotation rate of the spinning lid was $\omega = 2.387[rad\ s^{-1}]$ and the height of the container was increased to $H = 0.0375[m]$. The Reynolds number, 1492, and aspect ratio, $H/R = 1.5$, under these conditions were chosen to match the experimental study of Escudier[5].

While not shown here, the CFX-TASCflow results are in very good agreement with the flow visualizations, Figure A.1, reported by Escudier[5]. Table A.1 compares the predicted relative position of the stagnation points on
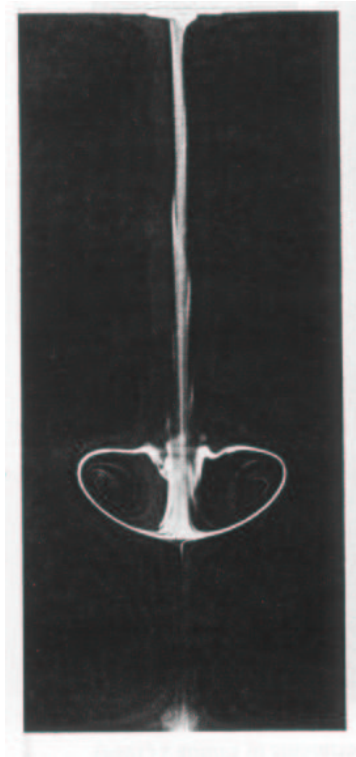
Figure A.1: Flow visualization of the centreline vortex as reported by Escudier[5].  The complete depth of the cylinder and the centre 34% of the diameter of the container is shown.

the centreline vortex with those measured in the experiments. The agreement is excellent.

| Stagnation Point | Experiment | Simulation |
|---|---|---|
| Upper | 0.39 | 0.38 |
| Lower | 0.27 | 0.27 |

Table A.1: Comparison of the predicted relative positions, $z/H$ of the upper and lower vortex stagnation points to those measured experimentally

## A.5   5: Turbulent Flow in a Container

The CFX-TASCFlow set up for this model flow was similar to that of Model Flow 4. The rotation rate of the lid was raised to $\omega = 400[rad\ s^{-1}]$ which was sufficient to create turbulent flow in the container.

The turbulent stresses were modeled with the standard $k-\varepsilon$ model. Wall functions were used to resolve the high velocity gradients in the near wall regions. All walls were modeled as smooth walls.

The time step was reduced to $0.01[s]$ to promote convergence.

# Appendix B

# Extra Shock Wave Model Flow Calculation

This appendix provides the details of the the simulation of the supersonic flow over the wedge airfoil that was performed with CFX-5.4.1. Three cases were simulated:

**Case 1:** constant viscosity air flow over no-slip airfoil surfaces,

**Case 2:** constant viscosity air flow over free slip airfoil surfaces, and

**Case 3:** temperature dependent viscosity air flow over no-slip airfoil surfaces.

Figure B.1 shows the two-dimensional geometry that was used for all three cases.

The wedge was $2[mm]$ long with an included angle of $10°$. The leading edge of the wedge was placed at the origin of the $x - y$ coordinate system. The solution domain extended $0.5[mm]$ forward from the leading edge and extended $2.0[mm]$ back from the trailing edge for a total length of $4.5[mm]$. The extension of the solution domain back from the trailing edge was required to ensure that approximations in the supersonic outflow boundary condition, especially in the vicinity of the trailing wake, do not affect accuracy or convergence. The solution domain extended upwards and downwards $2.0[mm]$ for a total height of $4.0[mm]$. This height was sufficient to ensure that any waves which were reflected off the top and bottom boundaries did not affect the solution in the region of interest around the leading edge tip. The solution domain had a depth of $0.02[mm]$. This thin depth was chosen so that the mesh was one layer of elements deep over most of the solution domain.
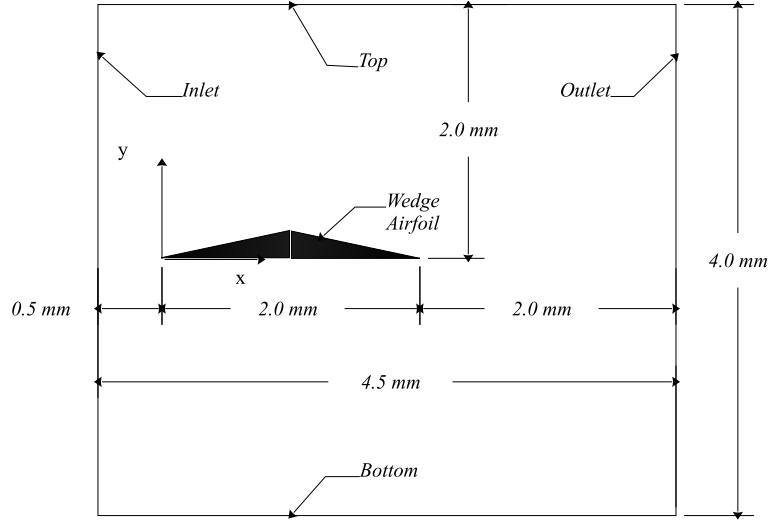
Figure B.1: Geometry for the CFX-5 simulation of flow over the supersonic wedge airfoil.

## B.1 Physical Models and Boundary Conditions

Air with a temperature of $293.2[K]$ and a pressure of $101325[Pa]$ flowed across the inflow surface shown in Figure B.1 at $673.3[m\ s^{-1}]$. With these properties, the Mach number of the flow before the wedge airfoil was 1.965. The air was modelled as a perfect gas with two viscosity models:

1. constant viscosity of $1.785 \times 10^{-5}[kg\ m^{-1}s^{-1}]$ (Cases 1 and 2), and

2. temperature dependent viscosity (Case 3) based on the Sutherland correlation:

$$\mu(T) = \mu_0 \left(\frac{T}{T_0}\right)^{\frac{3}{2}} \frac{T_0 + S_0}{T + S_0} \tag{B.1}$$

   where the reference conditions, $\mu_O$, $T_0$, and $S_0$, are $1.785\times10^{-5}[kg\ m^{-1}s^{-1}]$, $293.2[K]$, and $110[K]$, respectively.

The surfaces of the wedge were modelled as adiabatic surfaces with two fluid flow conditions:

1. no-slip (Cases 1 and 3), or

2. free slip (Case 2).

The latter was used to simulate inviscid flow over the wedge. The wedge airfoil was short enough that the boundary layer flow remained as laminar flow so no turbulence model was required.

The front, back, top, and bottom surfaces, shown in Figure B.1, were treated as symmetric plane surfaces. While this boundary condition causes artificial oblique reflections off the top and bottom surfaces, the reflected waves did no affect the flow field over the wedge.

A supersonic outlet boundary condition was applied to the outlet surface shown in Figure B.1. This condition allowed all flow properties and waves to leave the solution domain without disturbance. The minimum Mach number on the outlet surface was 1.58 for Cases 1 and 3 which indicates that the outlet surface was placed sufficiently far downstream to avoid subsonic flow at the outlet.

## B.2   Mesh

An isotropic unstructured mesh of tetrahedral elements was used over the solution domain. Over most of the solution domain, the average local mesh length was $0.02[mm]$. This background mesh length gave approximately 225 elements across the width of the domain, 200 elements across the height, and 1 element across the depth. The simulations for the inviscid flow over the free slip surfaces, Case 2, with this background mesh were virtually identical to those with a mesh length of $0.05[mm]$, except for the sharpness of the shock waves.

The background mesh length was much too large to resolve the features of the laminar boundary flows over the wedge no-slip surfaces. In the immediate vicinity of the no-slip surfaces, the mesh length was reduced to $0.002[mm]$ and then gradually expanded by an expansion factor of 1.2 until reaching the background mesh length. This refined mesh provided approximately 15 elements across the width of the laminar boundary layer on the wedge's bottom surface at $1.0[mm]$ back from the tip. Since the mesh remained isotropic, $750,000$ of the $800,000$ elements in the domain were in the very thin boundary layer regions. This limited the amount of mesh refinement in the boundary layer region.

## B.3   Discretization and Convergence Parameters

Over large regions of the flow domain the flow properties, such as velocity, pressure, and temperature, are uniform. Over isolated shock wave and

boundary layer regions, the flow properties change rapidly and are characterized by large gradients. As discussed above, a fine mesh was used to resolve the large gradients in the boundary layer regions. Since oblique shock waves have an almost infinitesimal thickness, a second order discretization scheme was used to ensure that the gradients were adequately resolved over the shock layers. The fringe plots presented in the main body show that simulated shock layers were very thin. While not obvious in the fringe plots, there were slight overshoots and undershoots in some flow properties in the regions of very steep gradients.

A timestep of $1.0 \times 10^{-5}[s]$ was used to control the iterative solution. This timestep was approximately 1.5 times the advection timescale for fluid to cross the width of the solution domain. With this timestep, approximately 60 iterations were required for each case to drive the maximum normalized residuals of all equations to below $1.0 \times 10^{-5}$.

## B.4   Computer Results

The calculations were carried out on an Intel_I386 architecture computer with Windows NT4.0 operating system. The following files are available:

**airfoil.db :** The geometry database used by CFX-Build.

**airfoil_001.out :** Summary of the CFX-Solver calculations for Case 1.

**airfoil_002.out :** Summary of the CFX-Solver calculations for Case 2.

**airfoil_003.out :** Summary of the CFX-Solver calculations for Case 3.

**airfoil_001.res :** The results files for Case 1.

**airfoil_002.res :** The results files for Case 2.

**airfoil_003.res :** The results files for Case 3.

**state.cst :** A state file for use in CFX-Post for setting up the processing used to generate the fringe plots and spreadsheets.

# Appendix C

# Corner Attraction Model Flow Calculation

This appendix provides the details of the simulations of fully-developed flow through a square duct that were performed with CFX-5.5.1 (some post-processing was done with CFX-5.6). Three cases involving incompressible air with nominal properties, density of $\rho = 1.284[kg/m^3]$ and dynamic viscosity of $\mu = 1.725 \times 10^{-5}[kg \ m^{-1}s^{-1}]$, were simulated:

**Case 1:** laminar flow with no turbulence model,

**Case 2:** turbulent flow with the eddy viscosity $k - \varepsilon$ turbulence model, and

**Case 3:** turbulent flow with the SSG form of the Reynolds Stress Transport model.

Figure C.1 shows the two-dimensional geometry that was used for all three cases. The duct had a half-width and half-height of $B = 0.025[m]$. The duct had a depth of $0.0025[m]$. This thin depth was chosen so that the mesh was only one layer of elements deep in the streamwise direction.

## C.1  Physical Models and Boundary Conditions

Because the flow in the square duct is symmetrical about each centre-plane, only the flow in the upper right quadrant was simulated. The leftsym and botsym surfaces, shown in Figure C.1, are centre-plane surfaces and were treated as symmetry plane surfaces. The rightwall and topwall surfaces were treated as smooth wall (no-slip) surfaces.

61

Figure C.1: Geometry for the CFX-5 simulation of fully-developed flow in square duct.

The flow is fully-developed so all flow properties, except pressure, do not change in the streamwise direction. Therefore, the surfaces inout1 and inout2 were treated as a periodic pair. Since this boundary condition implies that all fluid properties, including pressure, are periodic in the streamwise direction, it was necessary to specify a source term to account for the role of the streamwise pressure gradient. For fully developed flow in a duct with a hydraulic diameter, $2B$, the streamwise momentum source rate per unit volume, $\dot{S}_x$, (due to the streamwise pressure gradient)is

$$\dot{S}_x \equiv -\frac{\partial p}{\partial x} = \frac{2\tau_w}{B} \tag{C.1}$$

where $\tau_w$ is the wall shear stress. For a given fluid, the source term can be set to correspond to flow at a nominal Reynolds number based on hydraulic diameter, $Re_B \equiv \frac{2\rho B \bar{u}}{\mu}$ with the friction factor correlation for the wall shear stress:

$$\dot{S}_x = \frac{2\tau_w}{B} \tag{C.2}$$

$$= \frac{\rho \bar{u}^2 f(Re_B)}{4B} \tag{C.3}$$

$$= \quad \frac{\rho}{4B} \underbrace{\left[ \frac{\mu Re_B}{2\rho B} \right]^2}_{\bar{u}^2} f(Re_B) \qquad (C.4)$$

In the above, $\bar{u}$ is the cross-sectional average of the streamwise velocity. The friction factor correlations for smooth walled square ducts are based on the recommendations of White[22]:

$$f \quad \approx \quad \frac{57}{Re_B} \qquad\qquad\qquad Re_B < 2000 \qquad (C.5)$$

$$f \quad \approx \quad \left[ 1.8 \log_{10} \left( \frac{6.9}{Re_B} \right) \right]^{-2} \quad 4000 < Re_B \qquad (C.6)$$

The laminar flow simulations were based on a nominal Reynolds number of 1000 and the two turbulent flow simulations were based on a nominal Reynolds number of 65,000. Note that the actual Reynolds numbers were slightly different because of differences between the computational model and the friction factor correlation model.

For the turbulent flow simulations, two turbulence models were used for the Reynolds stresses:

$k - \varepsilon$ **Model:** The standard form of this eddy viscosity model was used.

**Reynolds Stress Transport Model (RSTM):** The crucial component is the model for the redistribution terms, $\Pi_{ij}$. The standard model of Rotta was used for the slow return to isotropy and the SSG model of Speziale *et al* [18] was used for the rapid process. This latter model was selected because of its improved ability to simulate anisotropy in turbulent flows, especially in near wall regions.

For both turbulent models, scalable wall functions were used to resolve the high velocity gradients in the near wall regions. The sensitivity of the simulated results to the details of the wall boundary conditions are discussed in the next sub-section.

## C.2   Mesh

A mesh with one element depth in the streamwise (periodic) direction was used. The results presented in the main body, were obtained with a 40 element by 40 element square uniform mesh in the cross-stream plane. This choice of mesh spacing was based on the results of a grid convergence study.

| Mesh | Nominal $y^+$ | $k - \varepsilon$ | | RSTM - SSG | |
|---|---|---|---|---|---|
| | | Standard | Scalable | Standard | Scalable |
| $10 \times 10$ | 160 | 0.0184 | 0.0182 | 0.0173 | 0.0171 |
| $20 \times 20$ | 80 | 0.0194 | 0.0181 | 0.0192 | 0.0177 |
| $40 \times 40$ | 40 | 0.0242 | 0.0181 | 0.0248 | 0.0179 |
| $80 \times 80$ | 20 | 0.0291 | 0.0183 | 0.0331 | 0.0179 |

Table C.1: Variation of predicted friction factor with number of mesh elements and corresponding near wall $y^+$ values. Results were obtained with $k - \varepsilon$ and RSTM-SSG turbulence models using both the standard and scalable wall function formulations.

Table C.1 shows the variation of the predicted friction factor with number of mesh elements (and corresponding value of $y^+$ for the first interior node off the wall) for the $k - \varepsilon$ and RSTM-SSG turbulence models. For each model, results were obtained with both the *standard* and *scalable* wall function formulations. For both turbulence models, the standard wall function formulation does not yield values which are grid converged. As the mesh is refined, the predicted friction factors increase significantly with decreasing mesh spacing. The scalable wall function formulation gives grid converged values for both turbulence models. A finer grid is required with the RSTM-SSG model than with the $k - \varepsilon$ model in order to provide sufficient resolution for the strong near wall gradients in the cross-stream (secondary) flow.

| Mesh | Nominal $y^+$ | $k - \varepsilon$ | | RSTM - SSG | |
|---|---|---|---|---|---|
| | | Standard | Scalable | Standard | Scalable |
| $10 \times 10$ | 160 | 1.20 | 1.19 | 1.18 | 1.18 |
| $20 \times 20$ | 80 | 1.20 | 1.20 | 1.19 | 1.18 |
| $40 \times 40$ | 40 | 1.22 | 1.19 | 1.22 | 1.18 |
| $80 \times 80$ | 20 | 1.25 | 1.19 | 1.25 | 1.18 |

Table C.2: Variation of centreline streamwise velocity divided by the mass average streamwise velocity with number of mesh elements and corresponding near wall $y^+$ values. Results were obtained with $k - \varepsilon$ and RSTM-SSG turbulence models using both the standard and scalable wall function formulations.

Table C.2 shows the variation of centreline streamwise velocity divided by mass average streamwise velocity, $\frac{u_{CL}}{\bar{u}}$, with number of mesh elements

for the same cases as presented in Table C.1. Again, the results show that the standard wall function formulation does not yield grid converged values. The prediction of $\frac{u_{CL}}{\bar{u}}$ does not show the same sensitivty to grid spacing as observed above for the friction factor, $f$.

## C.3 Discretization and Convergence Parameters

All simulations for the laminar and turbulent cases were obtained with the second order high resolution scheme applied to all transport equations.

Timesteps of $0.5[s]$ and $1.0 \times 10^{-3}[s]$ were used for the laminar and turbulent flow cases, respectively, to control the iterative solution. With these timesteps, approximately 160 iterations and 700 iterations were required for the laminar and turbulent cases, respectively, to drive the normalized root mean square(RMS) residuals of all equations to below $1.0 \times 10^{-6}$. While the convergence was slow (typical for periodic problems like this where the forcing velocity field is not directly set by the boundary conditions) the convergence was mostly monotonic.

## C.4 Comparison to Experiment and Other Simulations

Other experimental and numerical studies of the secondary turbulent flow in a square duct include:

**Brundrett and Baines[2] (B&B):** Pioneering experimental study of turbulent flow in a square duct. Measurements were performed on a flow with $Re_B = 83,000$.

**Gavrilakis[8] (G):** Direct numerical simulation was performed for flow at a $Re_B = 4,400$.

**Huser and Biringen[9] (H&B):** Direct numerical simulation was performed for flow at a $Re_B = 10,000$.

**Pettersson Reif and Andersson[14](P-R&A):** A Navier-Stokes solution based on the RSTM-SSG model. A high resolution treatment of the near wall region was used instead of the wall function formulation. Detailed results are presented for flow at a $Re_B = 10,000$ and friction factor results are presented for flow at $Re_B = 65,000$.

**Sata *et al*[15] (S,S,K&T):** Particle tracking velocimetry measurements
were made for flow at a $Re_B = 20,000$.

| Geometry | Experimenters | Model | $Re_B$ | $f_{Re_B=68,000}$ |
|---|---|---|---|---|
| Square Duct | - | CFX-5 RSTM-SSG | 68,000 | 0.018 |
| Square Duct | - | CFX-5 $k - \varepsilon$ | 68,000 | 0.018 |
| Square Duct | P-R& A | RSTM-SSG | 65,000 | 0.022 |
| Square Duct | H& B | DNS | 10,000 | 0.021 |
| Square Duct | B& B | Experiment | 83,000 | 0.017 |
| Round Pipe | Moody[22] | Experiment | 68,000 | 0.019 |

Table C.3: Comparison of friction factors to those measured or predicted by
other workers.

Table C.3 shows estimates of the friction factor obtained by various pre-
vious workers. Most of the previous work is at Reynolds numbers other
than 68,000. Reported friction factors have been adjusted to the equivalent
friction factor at a Reynolds number of 68,000 with the Haaland correla-
tion [22]:

$$f_{Re_B=68,000} \approx f_{\text{measured}} \left[ \frac{\log\left(\frac{6.9}{Re_B=\text{measured}}\right)}{\log\left(\frac{6.9}{Re_B=68,000}\right)} \right]^2 \qquad (C.7)$$

The agreement of the present prediction to previous experimental work in
round and square ducts is excellent. The agreement to previous numerical
estimates is reasonable given the uncertainty in the turbulence models.

| Geometry | Experimenters | Model | $Re_B$ | $\left(\frac{y_{VC}}{B}, \frac{z_{VC}}{B}\right)$ |
|---|---|---|---|---|
| Square Duct | - | CFX-5 RSTM-SSG | 68,000 | (0.78,0.46) |
| Square Duct | P-R& A | RSTM-SSG | 65,000 | (0.78,0.46) |
| Square Duct | H& B | DNS | 10,000 | (0.82,0.60) |
| Square Duct | G | DNS | 4,400 | (0.79,0.50) |
| Square Duct | S,S,K&T | Experiment | 20,000 | (0.83,0.44) |

Table C.4: Comparison of secondary flow vortex centre position to those
measured or predicted by other workers.

The shape of the secondary flow vortex is relatively insensitive to the
value of Reynolds number at higher Reynolds number,[9]. Table C.4 shows

estimates of the position of the vortex centre, $\left(\frac{y_{VC}}{B}, \frac{z_{VC}}{B}\right)$, obtained in various experimental and numerical studies. The agreement of the present prediction to previous work is excellent.
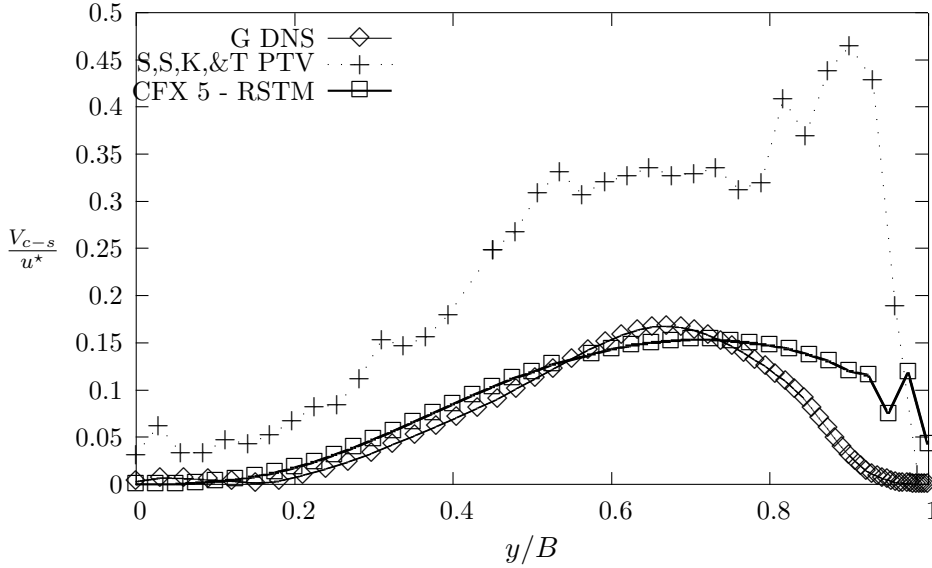


Figure C.2: Variation of normalized cross-stream flow speed, $V_{c-s}$, along the corner diagonal. Normalization is with respect to the wall shear velocity, $u^\star$. The $y$ coordinate is shown in Figure C.1.

When scaled by the wall shear velocity, $u^\star \equiv \sqrt{\tau_w/\rho}$, the cross-stream (secondary) velocity field, $V_{c-s} \equiv v(y,z)\hat{j} + w(y,z)\hat{k}$, is independent of the Reynolds number, $Re_B$, [9]. Figure C.2 shows the variation of the normalized cross-stream flow along the corner diagonal running from the duct centreline to the upper right corner. As shown in Figure 3.5c, the maximum speed of the cross-stream veloicty field occurs along this diagonal. Results are presented from the present study, the Direct Numerical Simulation (DNS) of Gavrilakis[8] for a low Reynolds number of 4,400, and for the experimental study of Sata *et al*[15] for a Reynolds number of 20,000. The present predictions for the strength of the cross-stream velocity field are under-predicted when compared to the experimental findings of Sata *et al*. This under-prediction can be attributed to the turbulence model and has been noted in other studies that use the Reynolds Stress Transport model, [14]. While the strength of the cross-stream velocity field is under-predicted,

the features of the variation along the diagonal, including the near corner dip and spike, are well predicted.

Overall, the agreement of the present predictions to known experimental results and to the numerical studies of previous workers is good.

## C.5   Computer Results

The calculations were carried out on an Intel_I386 architecture computer with Windows NT4.0 operating system. The following files are available:

**duct_laminar.out :** Summary of the CFX-Solver calculations for fully-developed laminar flow in a square duct with a $40 \times 40$ mesh, Case 1.

**duct_ke.out :** Summary of the CFX-Solver calculations for fully-developed turbulent flow in a square duct using the $k - \varepsilon$ turbulence model on a $40 \times 40$ mesh, Case 2.

**duct_rstm.out :** Summary of the CFX-Solver calculations for fully-developed turbulent flow in a square duct using the Reynolds stress transport model on a $40 \times 40$ mesh, Case 3.

**duct_laminar.res** The results file for Case 1.

**duct_ke.res** The results file for Case 2.

**duct_rstm.res** The results file for Case 3.

**SquareDuctData.xls :** Selected mean flow and Reynolds stress fields for Case 3 stored in Microsoft Excel format.

# Bibliography

[1] Bardsley, O. and Mair, W.A., 1951, *The Interaction between an Oblique Shock-wave and a Turbulent Boundary-layer.*, Philosophical Magazine, Vol. 42, pp. 29-36.

[2] Brundrett, E. and Baines, W.D., 1964, *The Production and Diffusion of Vorticity in a Square Duct*, Journal of Fluid Mechanics, Vol. 19, pp. 375-394.

[3] Daily, J.W. and Nece, R.E., 1960, *Chamber Dimension Effects on Induced Flow and Frictional Resistance of Enclosed Rotating Disks*, ASME Journal of Basic Engineering, Vol. 82, pp. 217-232.

[4] Eppler, R., 1990, *Airfoil Design and Data*, Springer-Verlag, Berlin.

[5] Escudier, M., 1984, *Observations of the Flow Produced in a Cylindrical Container By a Rotating Endwall*, Experiments in Fluids, Vol. 2, pp. 189-196.

[6] Escudier, M., 1987, *Confined Vortices in Flow Machinery*, Annual Review of Fluid Mechanics, Vol. 19, pp. 27-52.

[7] Escudier, M., 1988, *Vortex Breakdown: Observations and Explanations*, Progress in Aerospace Sciences, pp. 189-229.

[8] Gavrilakis, S., 1992, *Numerical Simulation of Low-Reynolds NUmber Flow Through a Straight Square Duct*, Journal of Fluid Mechanics, Vol. 244, pp. 101-129. Data is available at http://imhefwww.epfl.ch/lmf/research/gavrilakis/homepage.html.

[9] Huser, A. and Biringen, S., 1993, *Direct Numerical Simulation of Turbulent Flow in a Square Duct*, Journal of Fluid Mechanics, Vol. 257, pp. 65-95.

[10] Johnston, J.P., 1978, *Internal Flows*, in *Turbulence, Second Corrected and Updated Edition*, P.Bradshaw (ed.), Springer Verlag, Berlin, pp. 109-169.

[11] Lugt, H.J. and Haussling, H.J, 1973, *Development of Flow Circulation in a Rotating Tank*, Acta Mechanica, Vol. 18, pp. 255-272.

[12] Lugt, H.J., 1983, *Vortex Flows in Nature and Technology*, John Wiley and Sons, New York.

[13] Lugt, H.J., 1996, *Introduction to Vortex Theory*, Vortex Flow Press, Potomac, Maryland.

[14] Pettersson Reif, B.A. and Andersson, H.I., 2002, *Prediction of Turbulence-Generated Secondary Mean Flow in a Square Duct*, Flow, Turbulence, and Combustion, Vol. 68, pp. 41-61.

[15] Sata, Y., Sato, K., Kasagi, N., and Takamura, K., 1994, *Turbulent Air Flow Measurement with Three-Dimensional Particle Tracking Velocimetry*, Transactions of the Japanese Society of Mechanical Engineers, Series B, Vol. 60, pp. 865-871. Data available at http://www.thtlab.t.u-tokyo.ac.jp/PTV/fw_rc008.csv.

[16] Schlichting, H., 1979, *Boundary-Layer Theory, 7th. Edition*, McGraw-Hill, New York.

[17] Speziale, C.G., 1982, *On Turbulent Secondary Flow in Pipes of Noncircular Cross-Section*, International Journal of Engineering Science, Vol. 20, pp. 863 - 872.

[18] Speziale, C.G., Sarkar, S., and Gatski, T.B., 1991, *Modeling the Pressure-Strain Correlation of Turbulence: An Invariant Dynamical System Appproach*, Journal of Fluid Mechanics, Vol. 227, pp. 245-272.

[19] Stubley,G.D., 2001, *Finite Volume Solution of Similarity Equations for Rotating Flow over a Fixed Plate*, pp. 1-15, Mechanical Engineering Department, Waterloo.

[20] Van Dyke, M., 1982, *An Album of Fluid Motion*, The Parabolic Press, Stanford, California.

[21] White, F.M., 1991, *Viscous Fluid Flow, Second Edition*, McGraw-Hill, New York.

[22] White, F.M., 2003, *Fluid Mechanics, 5th edition*, McGraw-Hill, New York.